

On Probabilistic Pullback Metrics on Latent Hyperbolic Manifolds

Luis Augenstein¹ Noémie Jaquier^{1,2} Tamim Asfour¹ Leonel Rozo³

Abstract

Probabilistic Latent Variable Models (LVMs) have proven effective in capturing complex, high-dimensional data through lower-dimensional representations. Recent advances show that using Riemannian manifolds as latent spaces provides more flexibility to learn higher quality embeddings. This paper focuses on the hyperbolic manifold, a particularly suitable choice for modeling hierarchical relationships. Previous approaches relying on hyperbolic geodesics for interpolating the latent space often generate paths crossing low-data regions, leading to highly uncertain predictions. Instead, we propose augmenting the hyperbolic metric with a pullback metric to account for distortions introduced by the LVM’s nonlinear mapping and provide a complete development for pullback metrics of Gaussian Process LVMs (GPLVMs). Our experiments demonstrate that geodesics on the pullback metric not only respect the geometry of the hyperbolic latent space but also align with the underlying data distribution, significantly reducing uncertainty in predictions.

1. Introduction

Hyperbolic geometry is particularly useful in fields where data exhibits clear hierarchical structures, such as natural language processing for representing word hierarchies and taxonomies (Nickel & Kiela, 2017; 2018), as well as in social network analysis for modeling community structures (Krioukov et al., 2010; Doorenbos et al., 2024). Additionally, it finds applications in biology (Alanis-Lobato et al., 2018), human motion taxonomies (Jaquier et al., 2024), and computer vision (Khulkov et al., 2020). However, many datasets in these disciplines are high dimensional and heterogeneous, making latent variable models (LVMs) indispensable. Recently, hyperbolic embeddings gained significant attention due to their ability to capture hierarchical structures inherent in complex high-dimensional data (Skopek et al., 2020; Cho et al., 2023; Yang et al., 2023). These

¹Karlsruhe Institute of Technology ²KTH Royal Institute of Technology ³Bosch Center for AI.

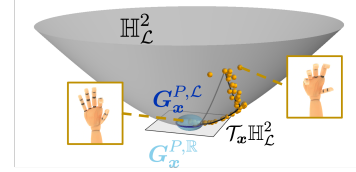


Figure 1: Hyperbolic pullback metric on the tangent space of the Lorentz model. The corresponding pullback geodesic (—) follow the data (•) manifold, in contrast to the hyperbolic geodesic (—).

embeddings leverage hyperbolic growth to accommodate hierarchical relationships, present in trees or graphs, that are difficult to model in Euclidean spaces (Cvetkovski & Crovella, 2009). Hyperbolic embeddings excel at preserving the hierarchical relationships of the original data in low-dimensional spaces (Sala et al., 2018). This can be achieved by leveraging a known taxonomy to guide the embedding process (Nickel & Kiela, 2017; Jaquier et al., 2024), by estimating the original data hierarchy via diffusion geometry (Lin et al., 2023), or by learning a tree on the original data (Sonthalia & Gilbert, 2020).

Despite the potential of hyperbolic embeddings, most of the state-of-the-art techniques operate without accounting for the intrinsic properties of the data. For example, the learned embeddings should be distance-preserving and their distribution should closely match that of the observed data. By doing so, any operation on the hyperbolic latent space complies with the properties of the data manifold. Instead, existing techniques generate geodesics that often traverse low-density regions of the data space, thus resulting in unrealistic interpolations and inaccurate representations. This problem of integrating the data manifold structure into latent spaces can be understood from a differential-geometry point-of-view (Hauberg, 2019) through stochastic pullback metrics (Tosi et al., 2014; Arvanitidis et al., 2018; 2021). This approach not only introduces uncertainty information into the latent space via the Riemannian metric, but also enables the generation of geodesics that faithfully follow the true data distribution. It has been leveraged in robot motion generation (Beik-Mohammadi et al., 2021), protein sequencing (Detlefsen et al., 2022), and data augmentation for medical imaging (Chadec et al., 2023). However, none of the aforementioned works considered hyperbolic geometry as inductive bias on the latent space.

This paper makes several key contributions to the field of

hyperbolic LVMs and GPLVMs. First, we introduce a general formulation of the Riemannian pullback metric on hyperbolic latent spaces, under the assumption of a stochastic latent-to-ambient mapping (see Fig. 1). Second, we present a novel development of the Riemannian pullback metric tailored to Gaussian Process Hyperbolic Latent Variable Models (GPHLVMs) (Jaquier et al., 2024), incorporating appropriate Riemannian projections onto tangent spaces to account for the hyperbolic geometry. Third, we develop the kernel derivatives within this setting, highlighting the limitations of current autodifferentiation techniques when applied to our setting. Finally, we demonstrate the benefits of hyperbolic pullback-based geodesics on four experiments: A proof-of-concept C-shape example, MNIST data interpolation, multi-cellular robot design (Dong et al., 2024), and human grasps generation (Jaquier et al., 2024).

2. Background

Riemannian geometry: Before delving into the hyperbolic manifold, it is necessary to establish a basic understanding in Riemannian geometry (Lee, 2018). A Riemannian manifold \mathcal{M} is a smooth manifold equipped with a Riemannian metric, i.e., a smoothly-varying inner product $g_x: \mathcal{T}_x\mathcal{M} \times \mathcal{T}_x\mathcal{M} \rightarrow \mathbb{R}$ over tangent spaces $\mathcal{T}_x\mathcal{M}$. When considering coordinates, the Riemannian metric is represented in matrix form for each $x \in \mathcal{M}$ as $\langle \mathbf{u}, \mathbf{v} \rangle_x = \mathbf{u}^\top \mathbf{G}_x \mathbf{v}$ with $\mathbf{u}, \mathbf{v} \in \mathcal{T}_x\mathcal{M}$. The Riemannian metric defines the length of curves in \mathcal{M} , leading to the notion of geodesics, defined as locally length-minimizing curves. To operate with Riemannian manifolds, it is common practice to exploit the Euclidean tangent spaces and the geodesics. The exponential map $\text{Exp}_x(\mathbf{u}) = \mathbf{y}$ maps $\mathbf{u} \in \mathcal{T}_x\mathcal{M}$ to a point $\mathbf{y} \in \mathcal{M}$, so that \mathbf{y} lies on a geodesic starting at x in the direction \mathbf{u} , and such that the geodesic distance $d_{\mathcal{M}}(x, \mathbf{y})$ equals the length of \mathbf{u} given by $\|\mathbf{u}\|_x = \sqrt{\langle \mathbf{u}, \mathbf{u} \rangle_x}$. The inverse operation is the logarithmic map $\text{Log}_x(\mathbf{y}) = \mathbf{u}$. Finally, the parallel transport $\Gamma_{x \rightarrow \mathbf{y}}(\mathbf{u}) = \mathbf{v}$ moves a vector $\mathbf{u} \in \mathcal{T}_x\mathcal{M}$ to $\mathcal{T}_\mathbf{y}\mathcal{M}$ while preserving the Riemannian inner product.

Optimizing manifold-valued functions requires generalizing the notion of gradient. The Riemannian gradient $\text{grad}_x(f)$ of a function $f: \mathcal{M} \rightarrow \mathbb{R}$ at $x \in \mathcal{M}$ is the unique tangent vector in $\mathcal{T}_x\mathcal{M}$ that satisfies $\mathcal{D}_\mathbf{u}f(x) = \langle \text{grad}_x f(x), \mathbf{u} \rangle_x$, where $\mathcal{D}_\mathbf{u}f(x)$ is the directional derivative of f in the direction $\mathbf{u} \in \mathcal{T}_x\mathcal{M}$ (Boumal, 2023, Chap. 3). The Riemannian Jacobian $\tilde{\mathbf{J}}$ of a function $f: \mathcal{M} \rightarrow \mathbb{R}^D$ is composed by the Riemannian gradients for each output dimension, i.e.,

$$\tilde{\mathbf{J}} = [\text{grad}_x(f_1) \dots \text{grad}_x(f_D)]^\top. \quad (1)$$

Hyperbolic Manifold: The hyperbolic manifold is the only Riemannian manifold with constant negative curvature (Ratcliffe, 2019). It is commonly represented by either the Poincaré model \mathbb{H}_ρ^D (Poincaré, 1900), employing lo-

cal coordinates within the unit ball, or the Lorentz model \mathbb{H}_ρ^D (Jansen, 1909; Reynolds, 1993), using Cartesian coordinates to represent the surface embedded in \mathbb{R}^{D+1} . In this paper we mostly rely on the latter, which is numerically more stable and defined as,

$$\mathbb{H}_\rho^D = \{\mathbf{x} \in \mathbb{R}^{D+1} \mid \langle \mathbf{x}, \mathbf{x} \rangle_{\mathcal{L}} = -1, x_0 > 0\}, \quad (2)$$

where $\langle \mathbf{x}, \mathbf{y} \rangle_{\mathcal{L}} = \mathbf{x}^\top \mathbf{G}^{\mathcal{L}} \mathbf{y}$ is the Lorentzian inner product with $\mathbf{G}^{\mathcal{L}} = \text{diag}(-1, 1, \dots, 1)$. Further details on the hyperbolic manifold and its operations are provided in App. A.

Gaussian Process Hyperbolic Latent Variable Model (GPHLVM): A GPLVM defines a generative mapping from latent variables $\mathbf{x}_n \in \mathbb{R}^{D_x}$ to observations $\mathbf{y}_n \in \mathbb{R}^{D_y}$ with $D_x < D_y$ through a non-linear transformation modeled by Gaussian processes (GPs) (Lawrence, 2003). A GPLVM assumes that the observations are normally distributed, i.e., $y_{n,d} \sim \mathcal{N}(f_{n,d}, \sigma_y^2)$, and described via a GP and a prior,

$$f_{n,d} \sim \text{GP}(0, k(\mathbf{x}_n, \mathbf{x}_n)) \quad \text{and} \quad \mathbf{x}_n \sim \mathcal{N}(\mathbf{0}, \mathbf{I}), \quad (3)$$

where $y_{n,d}$ is the d -th dimension of \mathbf{y}_n , $k: \mathbb{R}^{D_x} \times \mathbb{R}^{D_x} \rightarrow \mathbb{R}$ is the GP kernel function which measures the similarity between two inputs $\mathbf{x}_n, \mathbf{x}_m$, and σ_y^2 is the noise variance.

In some cases, a Euclidean latent space may not necessarily comply with structural biases in the observed data, and therefore curved geometries such as the hyperbolic manifold may be preferred. In such cases, the latent variables $\mathbf{x}_n \in \mathbb{H}_\rho^{D_x}$ live in a hyperbolic space and the generative mapping is defined via a GPHLVM (Jaquier et al., 2024). Consequently the kernel function in (3) is replaced by a hyperbolic kernel $k^{\mathbb{H}_\rho^{D_x}}: \mathbb{H}_\rho^{D_x} \times \mathbb{H}_\rho^{D_x} \rightarrow \mathbb{R}$ as introduced shortly. Moreover, the latent variables are assigned a hyperbolic wrapped Gaussian prior $\mathbf{x}_n \sim \mathcal{N}_{\mathbb{H}_\rho^{D_x}}(\boldsymbol{\mu}_0, \alpha \mathbf{I})$, with $\boldsymbol{\mu}_0 = (1, 0, \dots, 0)^\top$ and α controlling the spread of the latent variables (see App. A for more details). The GPHLVM latent variables and hyperparameters are inferred by finding a MAP estimate or via variational inference similar as in the Euclidean case.

Hyperbolic Kernels: The SE and Matérn kernels are standard choices when designing GPs (Rasmussen & Williams, 2006). These kernels have been recently generalized to non-Euclidean spaces such as manifolds (Borovitskiy et al., 2020; Jaquier et al., 2021), or graphs (Borovitskiy et al., 2021). Grigoryan & Noguchi (1998) demonstrated that, in hyperbolic space, 2- and 3-dimensional SE kernels suffice since higher-dimensional kernels can be expressed as derivatives of these lower-dimensional ones. The 2D and 3D hyperbolic SE kernels are given as,

$$k^{\mathbb{H}_\rho^2}(\mathbf{x}, \mathbf{z}) = \frac{\tau}{C_\infty} \int_\rho^\infty \frac{s e^{-\frac{s^2}{2\kappa^2}}}{\sqrt{\cosh(s) - \cosh(\rho)}} ds, \quad (4)$$

$$k^{\mathbb{H}_\rho^3}(\mathbf{x}, \mathbf{z}) = \frac{\tau}{C_\infty} \frac{\rho}{\sinh(\rho)} e^{-\frac{\rho^2}{2\kappa^2}}, \quad (5)$$

where $\rho = d_{\mathbb{H}_{\mathcal{L}}^{D_x}}(\mathbf{x}, \mathbf{z})$ is the geodesic distance between $\mathbf{x}, \mathbf{z} \in \mathbb{H}_{\mathcal{L}}^{D_x}$, $\tau, \kappa \in \mathbb{R}_+$ are the kernel variance and length-scale, and C_∞ is a normalization constant. As no closed form solution is known in the 2D case, the kernel needs to be approximated via a discretization of the integral in (4). We use the positive semidefinite Monte Carlo approximation introduced by Jaquier et al. (2024),

$$k_{\mathbb{H}_{\mathcal{L}}^2}(\mathbf{x}, \mathbf{z}) \approx \frac{\tau}{C_\infty} \frac{1}{L} \sum_{l=1}^L s_l \tanh(\pi s_l) \Phi_l(\mathbf{x}_{\mathcal{P}}, \mathbf{z}_{\mathcal{P}}), \quad (6)$$

where $\Phi_l(\mathbf{x}_{\mathcal{P}}, \mathbf{z}_{\mathcal{P}}) = \phi_l(\mathbf{x}_{\mathcal{P}}) \bar{\phi}_l(\mathbf{z}_{\mathcal{P}})$ is the only component depending on the kernel inputs, $\bar{\phi}_l$ is the complex conjugate of $\phi_l(\mathbf{x}_{\mathcal{P}}) = e^{(1+2s_l i)\langle \mathbf{x}_{\mathcal{P}}, \mathbf{b}_l \rangle}$, $\mathbf{x}_{\mathcal{P}} \in \mathbb{H}_{\mathcal{P}}^{D_x}$ is the Poincaré representation of \mathbf{x} , $\mathbf{b}_l \sim U(\mathbb{S}^1)$ are samples from the unit circle, $s_l \sim e^{-\frac{s^2 \kappa^2}{2}} 1_{[0, \infty)}(s)$ are samples from a truncated Gaussian distribution, and $\langle \mathbf{x}_{\mathcal{P}}, \mathbf{b} \rangle = \frac{1}{2} \log \left(\frac{1 - |\mathbf{x}_{\mathcal{P}}|^2}{|\mathbf{x}_{\mathcal{P}} - \mathbf{b}|^2} \right)$ is the hyperbolic outer product.

Pullback metrics: Consider an immersion $f: \mathcal{S} \rightarrow \mathcal{M}$ from a latent space \mathcal{S} to a Riemannian manifold \mathcal{M} equipped with a Riemannian metric g_y . The immersion f induces a pullback metric $g_x^{\mathcal{P}}$ on \mathcal{S} which, for $\mathbf{x} \in \mathcal{S}$ and $\mathbf{u}, \mathbf{v} \in \mathcal{T}_{\mathbf{x}}\mathcal{S}$, is given by (Lee, 2018, Chap. 2)

$$g_x^{\mathcal{P}}(\mathbf{u}, \mathbf{v}) = g_{f(\mathbf{x})}(df_{\mathbf{x}}(\mathbf{u}), df_{\mathbf{x}}(\mathbf{v})). \quad (7)$$

With coordinates, the pullback metric is given in matrix form by $\mathbf{G}_x^{\mathcal{P}} = \tilde{\mathbf{J}}^T \mathbf{G}_y \tilde{\mathbf{J}}$, where $\tilde{\mathbf{J}}$ is the Riemannian Jacobian (1) of f at \mathbf{x} . Intuitively, $g_x^{\mathcal{P}}$ evaluates on tangent vectors of $\mathcal{T}_{\mathbf{x}}\mathcal{S}$ by moving them to $\mathcal{T}_{f(\mathbf{x})}\mathcal{M}$ to compute their inner product. For an immersion $f: \mathcal{S} \rightarrow \mathbb{R}^{D_y}$ with Euclidean co-domain, i.e., $\mathbf{G}_y = \mathbf{I}$, the pullback metric is $\mathbf{G}_x^{\mathcal{P}} = \tilde{\mathbf{J}}^T \tilde{\mathbf{J}}$. For Euclidean domains $\mathcal{S} = \mathbb{R}^{D_x}$, $\tilde{\mathbf{J}}$ equals the Euclidean Jacobian $\mathbf{J} = [\frac{\partial f_1}{\partial \mathbf{x}} \dots \frac{\partial f_{D_y}}{\partial \mathbf{x}}]^T \in \mathbb{R}^{D_y \times D_x}$. In this paper, we define pullback metrics of hyperbolic LVMs by explicitly leveraging immersions $f: \mathbb{H}^{D_x} \rightarrow \mathbb{R}^{D_y}$, where f is a GPHLVM.

3. Metrics of Hyperbolic LVMs

Tosi et al. (2014) introduced the pullback metric for Euclidean GPLVMs and its use to compute geodesics that adhere to the data distribution. Here, we extend this approach to hyperbolic LVMs, specifically to the GPHLVM introduced in Sec. 2. We show that the resulting metric can be computed similarly to the Euclidean case, with two key exceptions: (1) the pullback metric must be adequately projected onto appropriate tangent spaces; and (2) the computation of the derivatives for the hyperbolic SE kernels is significantly more challenging than in the Euclidean scenario.

3.1. A General Hyperbolic Pullback Metric

A deterministic immersion $f: \mathbb{R}^{D_x} \rightarrow \mathbb{R}^{D_y}$ pulls back the metric into the latent space following (7), i.e., $\mathbf{G}_x^{\mathcal{P}, \mathbb{R}} = \mathbf{J}^T \mathbf{J}$.

In the context of LVMs, the immersion f is stochastic. As developed in (Tosi et al., 2014), the stochastic immersion f induces a distribution over its Jacobian \mathbf{J} , which itself induces a distribution over the pullback metric. As Tosi et al. (2014), we consider LVMs for which the probability over \mathbf{J} follows a Gaussian distribution. Assuming independent rows $\mathbf{J}_d \in \mathbb{R}^{D_x}$, each with its own mean but shared covariance matrix, the Jacobian distribution is of the form,

$$p(\mathbf{J}) = \prod_{d=1}^{D_y} \mathcal{N}(\mathbf{J}_d | \boldsymbol{\mu}_d, \boldsymbol{\Sigma}_J). \quad (8)$$

Therefore, the metric tensor $\mathbf{G}_x^{\mathcal{P}, \mathbb{R}}$ follows a non-central Wishart distribution (Anderson, 1946),

$$p(\mathbf{G}_x^{\mathcal{P}, \mathbb{R}}) = \mathcal{W}_{D_x}(D_y, \boldsymbol{\Sigma}_J, \mathbb{E}[\mathbf{J}]^T \mathbb{E}[\mathbf{J}]), \quad (9)$$

which we compute the expected metric tensor from,

$$\mathbb{E}[\mathbf{G}_x^{\mathcal{P}, \mathbb{R}}] = \mathbb{E}[\mathbf{J}]^T \mathbb{E}[\mathbf{J}] + D_y \boldsymbol{\Sigma}_J. \quad (10)$$

While the hyperbolic case follows a similar strategy, special care is required to ensure that the Jacobian rows lie on appropriate tangent spaces. A hyperbolic LVM defines a stochastic mapping $f: \mathbb{H}_{\mathcal{L}}^{D_x} \rightarrow \mathbb{R}^{D_y}$, whose Jacobian is computed from the Riemannian gradients of f as in (1). As for Riemannian submanifolds (Boumal, 2023), each Riemannian gradient $\text{grad}_{\mathbf{x}}(f_d)$ equals the orthogonal projection of the Euclidean gradient $\frac{\partial f_d}{\partial \mathbf{x}} \in \mathbb{R}^{D_x+1}$ onto $\mathcal{T}_{\mathbf{x}}\mathbb{H}_{\mathcal{L}}^{D_x}$,

$$\text{grad}_{\mathbf{x}}(f_d) = \text{proj}_{\mathbf{x}} \left(\frac{\partial f_d}{\partial \mathbf{x}} \right) = \mathbf{P}_x \frac{\partial f_d}{\partial \mathbf{x}}, \quad (11)$$

with $\mathbf{P}_x = \mathbf{G}^{\mathcal{L}} + \mathbf{x}\mathbf{x}^T$. Therefore, the Riemannian Jacobian $\tilde{\mathbf{J}}$ is computed from the Euclidean Jacobian \mathbf{J} as $\tilde{\mathbf{J}} = [\mathbf{P}_x \frac{\partial f_1}{\partial \mathbf{x}} \dots \mathbf{P}_x \frac{\partial f_{D_y}}{\partial \mathbf{x}}]^T = \mathbf{J} \mathbf{P}_x^T$. Assuming independent rows $\tilde{\mathbf{J}}_d$ as in the Euclidean case, the Jacobian distribution is computed from (8) as (Bishop, 2006, Chap. 2.3),

$$p(\tilde{\mathbf{J}}) = \prod_{d=1}^{D_y} \mathcal{N}(\tilde{\mathbf{J}}_d | \mathbf{P}_x \boldsymbol{\mu}_d, \mathbf{P}_x \boldsymbol{\Sigma}_J \mathbf{P}_x^T). \quad (12)$$

Similarly to $\mathbf{G}_x^{\mathcal{P}, \mathbb{R}}$ in (9), the metric tensor $\mathbf{G}_x^{\mathcal{P}, \mathcal{L}}$ follows a non-central Wishart distribution (Anderson, 1946),

$$p(\mathbf{G}_x^{\mathcal{P}, \mathcal{L}}) = \mathcal{W}_{D_x}(D_y, \tilde{\boldsymbol{\Sigma}}_J, \mathbb{E}[\tilde{\mathbf{J}}]^T \mathbb{E}[\tilde{\mathbf{J}}]), \quad (13)$$

with $\tilde{\boldsymbol{\Sigma}}_J = \mathbf{P}_x \boldsymbol{\Sigma}_J \mathbf{P}_x^T$, leading to the expected metric,

$$\begin{aligned} \mathbb{E}[\mathbf{G}_x^{\mathcal{P}, \mathcal{L}}] &= \mathbb{E}[\tilde{\mathbf{J}}]^T \mathbb{E}[\tilde{\mathbf{J}}] + D_y \tilde{\boldsymbol{\Sigma}}_J \\ &= \mathbf{P}_x (\mathbb{E}[\mathbf{J}]^T \mathbb{E}[\mathbf{J}] + D_y \boldsymbol{\Sigma}_J) \mathbf{P}_x^T. \end{aligned} \quad (14)$$

Intuitively, the pullback metric $\mathbf{G}_x^{\mathcal{P}, \mathcal{L}}$ is the orthogonal projection of the Euclidean pullback metric $\mathbf{G}_x^{\mathcal{P}, \mathbb{R}}$ onto the tangent space $\mathcal{T}_{\mathbf{x}}\mathbb{H}_{\mathcal{L}}^{D_x}$ (see Fig. 1). It relates to the hyperbolic metric $\mathbf{G}^{\mathcal{L}}$ via the projection \mathbf{P}_x , which is orthogonal with respect to the Lorentzian inner product.

3.2. The GPLVM Pullback Metric

Here, we consider the case where the mapping f is defined as a GPLVM. We derive the distribution of the Riemannian Jacobian, which we then use to compute the expected GPLVM pullback metric $\mathbf{G}_{\mathbf{x}^*}^{\mathcal{P},\mathcal{L}}$. As for GPLVMs (Tosi et al., 2014), the joint distribution of the Jacobian $\tilde{\mathbf{J}}$ and observations $\mathbf{Y} = [\mathbf{y}_1 \dots \mathbf{y}_N]^\top \in \mathbb{R}^{N \times D_y}$ is given as,

$$\mathcal{N} \left(\begin{bmatrix} \mathbf{Y}_d \\ \tilde{\mathbf{J}}_d \end{bmatrix} \middle| \begin{bmatrix} \mathbf{0} \\ \mathbf{0} \end{bmatrix}, \begin{bmatrix} \mathbf{K}_X + \sigma_y^2 \mathbf{I}_N & \partial k(\mathbf{X}, \mathbf{x}^*) \\ \partial k(\mathbf{x}^*, \mathbf{X}) & \partial^2 k(\mathbf{x}^*, \mathbf{x}^*) \end{bmatrix} \right), \quad (15)$$

where $\mathbf{X} = [\mathbf{x}_1 \dots \mathbf{x}_N]^\top \in \mathbb{R}^{N \times (D_x+1)}$ with $\mathbf{x}_n \in \mathbb{H}_{\mathcal{L}}^{D_x}$, $\mathbf{K}_X \in \mathbb{R}^{N \times N}$ is the corresponding kernel matrix, \mathbf{Y}_d denotes the d -th row of \mathbf{Y} , and we rely on the hyperbolic kernel derivatives,

$$\partial k(\mathbf{X}, \mathbf{x}^*) = \frac{\partial}{\partial \mathbf{z}} k(\mathbf{X}, \mathbf{z}) \Big|_{\mathbf{z}=\mathbf{x}^*}, \quad (16)$$

$$\partial^2 k(\mathbf{x}^*, \mathbf{x}^*) = \frac{\partial^2}{\partial \mathbf{z} \partial \mathbf{x}} k(\mathbf{x}, \mathbf{z}) \Big|_{\mathbf{x}=\mathbf{z}=\mathbf{x}^*}. \quad (17)$$

While in the Euclidean case the kernel derivatives are straightforward, the hyperbolic setting is more challenging, as will be discussed in Sec. 4. Conditioning on the observations $\mathbf{Y}_d \in \mathbb{R}^N$ results in the probability distribution of the Jacobian at \mathbf{x}^* (Bishop, 2006, Chap 2.3),

$$p(\tilde{\mathbf{J}} \mid \mathbf{Y}, \mathbf{X}, \mathbf{x}_*) = \prod_{d=1}^{D_y} \mathcal{N}(\tilde{\mathbf{J}}_d \mid \boldsymbol{\mu}_d, \boldsymbol{\Sigma}_J), \quad (18)$$

$$\text{with } \boldsymbol{\mu}_d = \mathbf{S}_J \mathbf{Y}_d, \quad (19)$$

$$\boldsymbol{\Sigma}_J = \partial^2 k(\mathbf{x}^*, \mathbf{x}^*) - \mathbf{S}_J \partial k(\mathbf{X}, \mathbf{x}^*), \quad (20)$$

$$\mathbf{S}_J = \partial k(\mathbf{x}^*, \mathbf{X}) (\mathbf{K}_X + \sigma_y^2 \mathbf{I}_N)^{-1}. \quad (21)$$

The expected pullback metric is computed using (14) as,

$$\mathbb{E}[\mathbf{G}_{\mathbf{x}^*}^{\mathcal{P},\mathcal{L}}] = \mathbf{P}_{\mathbf{x}^*} (\boldsymbol{\mu}_J^\top \boldsymbol{\mu}_J + D_y \boldsymbol{\Sigma}_J) \mathbf{P}_{\mathbf{x}^*}^\top, \quad (22)$$

with $\boldsymbol{\mu}_J = [\boldsymbol{\mu}_1 \dots \boldsymbol{\mu}_{D_y}]^\top \in \mathbb{R}^{D_y \times D_x}$.

3.3. Hyperbolic Pullback Geodesics

Having endowed the hyperbolic latent space with a pullback metric $\mathbf{G}^{\mathcal{P},\mathcal{L}}$, we are now interested in computing shortest paths, i.e., geodesics, between latent hyperbolic points. While hyperbolic geodesics have a closed-form solution, they may not always align with the underlying data distribution (see Fig. 2). Instead, hyperbolic pullback geodesics naturally follow the data distribution, but require solving an optimization problem. Specifically, pullback geodesics are computed by minimizing the curve length, or equivalently the curve energy E with respect to the pullback metric. When considering a discretized geodesic composed by a set of M points $\mathbf{x}_i \in \mathbb{H}_{\mathcal{L}}^{D_x}$, this boils down to minimize,

$$E = \sum_{i=0}^{M-2} \mathbf{v}_i^\top \mathbf{G}_{\mathbf{x}_i}^{\mathcal{P},\mathcal{L}} \mathbf{v}_i, \quad \text{with } \mathbf{v}_i = \text{Log}_{\mathbf{x}_i}(\mathbf{x}_{i+1}). \quad (23)$$

Table 1: Average computation times in seconds over 100 runs, each evaluating the pullback metric $\mathbf{G}_{\mathbf{x}^*}^{\mathcal{P},\mathcal{L}}$ and its derivatives at a random point \mathbf{x} . PyTorch fails to compute the 3D kernel derivatives.

	$k^{\mathbb{H}_{\mathcal{L}}^2}$ ($L = 3000$) (6)	$k^{\mathbb{H}_{\mathcal{L}}^3}$ (5)
PYTORCH DERIVATIVES	0.83 ± 0.06	–
CUSTOM DERIVATIVES	0.16 ± 0.02	0.06 ± 0.01

While it is possible to iteratively optimize the curve points \mathbf{x}_i directly, this often leads to uneven spacing among them. This issue can be addressed either by using a parametric curve on the manifold (Gousenbourger et al., 2014) and optimize its parameters instead of the points directly, or by incorporating the spline energy as a regularization factor in the optimization process (Heeren et al., 2018). We follow the latter. The spline energy is $E_{\text{spline}} \approx \sum_{i=1}^{M-2} d_{\mathbb{H}_{\mathcal{L}}^{D_x}}(\mathbf{x}_i, \bar{\mathbf{x}}_i)^2$, where $\bar{\mathbf{x}}_i = \text{Exp}_{\mathbf{x}_{i-1}}\left(\frac{1}{2} \text{Log}_{\mathbf{x}_{i-1}}(\mathbf{x}_{i+1})\right)$ is the geodesic midpoint between \mathbf{x}_{i-1} and \mathbf{x}_{i+1} . The final optimization problem is,

$$\min_{\mathbf{x}_0, \dots, \mathbf{x}_{M-1}} E + \lambda E_{\text{spline}}, \quad (24)$$

with λ weighting the influence of the regularization. As the optimization parameters are Riemannian, we leverage Riemannian optimizers such as Riemannian Adam (Bécigneul & Ganea, 2019) to optimize (23). The computation of pullback geodesics is summarised by Algorithm 1 in App. C.

4. Hyperbolic Kernel Derivatives

In this section, we discuss the challenges encountered when using autodiff tools, in particular PyTorch (Paszke et al., 2019), to compute the derivatives of the hyperbolic SE kernels. Table 1 shows that autodiff-based kernel derivatives are approximately five times slower than custom analytic implementations in the 2D case. More importantly, in the 3D case, autodiff fails to compute the derivatives entirely.

4.1. 2D Hyperbolic SE Kernel Derivatives

We compute the 2D hyperbolic SE kernel $k^{\mathbb{H}_{\mathcal{L}}^2}(\mathbf{x}, \mathbf{z})$ via the Monte Carlo approximation (6). The pullback metric tensor $\mathbf{G}_{\mathbf{x}^*}^{\mathcal{P},\mathcal{L}}$ is computed using the kernel derivatives $\frac{\partial}{\partial \mathbf{x}} k(\mathbf{x}, \mathbf{z})|_{\mathbf{x}=\mathbf{x}^*}$ (16) and $\frac{\partial^2}{\partial \mathbf{z} \partial \mathbf{x}} k(\mathbf{x}, \mathbf{z})|_{\mathbf{x}=\mathbf{z}=\mathbf{x}^*}$ (17). The only part of the kernel (6) that depends on the inputs \mathbf{x}, \mathbf{z} is the function $\Phi_l(\mathbf{x}, \mathbf{z})$, whose derivatives are given by,

$$\frac{\partial}{\partial \mathbf{x}} \Phi_l(\mathbf{x}, \mathbf{z}) = \left[\frac{\partial}{\partial \mathbf{x}} \phi_l(\mathbf{x}_P) \right] \bar{\phi}_l(\mathbf{z}_P), \quad (25)$$

$$\frac{\partial^2}{\partial \mathbf{z} \partial \mathbf{x}} \Phi_l(\mathbf{x}, \mathbf{z}) = \left[\frac{\partial}{\partial \mathbf{x}} \phi_l(\mathbf{x}_P) \right] \left[\frac{\partial}{\partial \mathbf{z}} \bar{\phi}_l(\mathbf{z}_P) \right]^\top. \quad (26)$$

The kernel derivatives (16)-(17) are thus straightforwardly determined from (25)-(26), and subsequently leveraged to compute $\mathbf{G}_{\mathbf{x}^*}^{\mathcal{P},\mathcal{L}}$ using (22). Minimizing the curve energy (23) to compute pullback geodesics additionally requires the

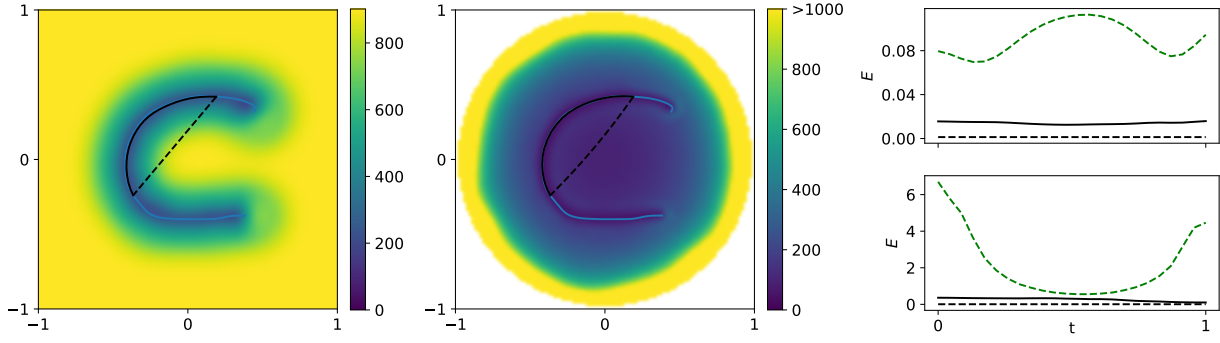


Figure 2: *Left and middle*: Euclidean and hyperbolic pullback metrics on a C-shape trajectory (—). The geodesics of the base manifold (---) and the pullbacks geodesic (—) are depicted on both Euclidean and hyperbolic spaces. *Right*: Curve energy along the geodesics on the Euclidean (top) and hyperbolic (bottom) cases. These include the base manifold geodesic (---), the base manifold geodesic with energy (23) evaluated using the pullback metric (-.-), and the pullback geodesic (—).

derivative $\frac{\partial}{\partial \mathbf{x}^*} \mathbf{G}_{\mathbf{x}^*}^{\mathcal{P}, \mathcal{L}}$. This, in turn, requires the derivative of the Jacobian of the covariance matrix $\frac{\partial}{\partial \mathbf{x}^*} \Sigma_J$, which depends on the kernel derivatives $\frac{\partial^3}{\partial \mathbf{x} \partial \mathbf{z} \partial \mathbf{x}} k(\mathbf{x}, \mathbf{z})|_{\mathbf{x}=\mathbf{z}=\mathbf{x}^*}$, and $\frac{\partial^3}{\partial \mathbf{z}^2 \partial \mathbf{x}} k(\mathbf{x}, \mathbf{z})|_{\mathbf{x}=\mathbf{z}=\mathbf{x}^*}$. Again, the kernel derivatives are effectively determined by the derivatives of $\Phi_l(\mathbf{x}, \mathbf{z})$,

$$\frac{\partial^3}{\partial \mathbf{x} \partial \mathbf{z} \partial \mathbf{x}} \Phi_l(\mathbf{x}, \mathbf{z}) = \left[\frac{\partial^2}{\partial \mathbf{x}^2} \phi_l(\mathbf{x}_{\mathcal{P}}) \right] \times_2 \left[\frac{\partial}{\partial \mathbf{z}} \bar{\phi}_l(\mathbf{z}_{\mathcal{P}}) \right], \quad (27)$$

$$\frac{\partial^3}{\partial \mathbf{z}^2 \partial \mathbf{x}} \Phi_l(\mathbf{x}, \mathbf{z}) = \left[\frac{\partial^2}{\partial \mathbf{z}^2} \bar{\phi}_l(\mathbf{z}_{\mathcal{P}}) \right] \times_1 \left[\frac{\partial}{\partial \mathbf{x}} \phi_l(\mathbf{x}_{\mathcal{P}}) \right], \quad (28)$$

where $\mathbf{A} \times_i \mathbf{B}$ refers to n-mode product (Kolda & Bader, 2009b) which multiplies the i -th dimension of \mathbf{A} with the second dimension of \mathbf{B} . If \mathbf{B} is a vector, \mathbf{A} is unsqueezed at dimension i before the multiplication. The matrices $\frac{\partial^2}{\partial \mathbf{x}^2} \phi_l(\mathbf{x}_{\mathcal{P}}), \frac{\partial^2}{\partial \mathbf{z}^2} \bar{\phi}_l(\mathbf{z}_{\mathcal{P}}) \in \mathbb{R}^{3 \times 3}$ in (27)-(28) are therefore interpreted as $\mathbb{R}^{3 \times 1 \times 3}$ and $\mathbb{R}^{1 \times 3 \times 3}$, respectively. The complete derivation of all derivatives is provided in App. B.

4.2. 3D Hyperbolic SE Kernel Derivatives

The 3D hyperbolic SE kernel is given by (5). In this section, we simplify its notation and write $k(\mathbf{x}, \mathbf{z}) = \frac{\rho}{s} e^{-\frac{\rho^2}{s}}$ by omitting the constant τ/C_∞ , setting $\nu = 2\kappa^2$, and introducing the helper variables $u = \langle \mathbf{x}, \mathbf{z} \rangle_{\mathcal{L}}$ and $s = \sqrt{u^2 - 1}$. As in the 2D case, to obtain the expected pullback metric tensor (22), we compute the first two kernel derivatives,

$$\frac{\partial}{\partial \mathbf{x}} k(\mathbf{x}, \mathbf{z}) = g(u) \mathbf{G}^{\mathcal{L}} \mathbf{z} e^{-\frac{\rho^2}{s}}, \quad (29)$$

$$\frac{\partial^2}{\partial \mathbf{z} \partial \mathbf{x}} k(\mathbf{x}, \mathbf{z}) = (h(u) \mathbf{G}^{\mathcal{L}} \mathbf{z} \mathbf{x}^{\top} \mathbf{G}^{\mathcal{L}} + g(u) \mathbf{G}^{\mathcal{L}}) e^{-\frac{\rho^2}{s}}, \quad (30)$$

with $g(u) = \left(\frac{2\rho^2}{\nu s^2} - \frac{1}{s^2} - \frac{u\rho}{s^3} \right)$ and $h(u) = \frac{d}{du} g(u) + \frac{g(u)2\rho}{\nu s}$. The helper functions $g(u)$ and $h(u)$ are essential to understand why standard autodiff tools fail to compute the derivatives (29)-(30). For equal inputs $\mathbf{x} = \mathbf{z}$, the inner product u

approaches -1 , while the distance $\rho = d_{\mathbb{H}^{\mathcal{L}}_x}(\mathbf{x}, \mathbf{z})$ and variable s converge to 0. This limit is analytically well behaved for the helper functions, e.g., $\lim_{u \rightarrow -1^-} g(u) = \frac{2}{\nu} + \frac{1}{3}$. However, autodiff tools fail to compute the kernel derivatives for equal inputs correctly because they do not cancel out 0-approaching terms. For example, we have for $g(u)$,

$$\frac{2\rho^2}{\nu s^2} - \frac{1}{s^2} - \frac{u\rho}{s^3} \xrightarrow{\text{autodiff}} \frac{0}{0} - \frac{1}{0} - \frac{0}{0} = \text{NaN}.$$

In this scenario, autodiff divides by 0, leading to undefined values (NaN). In other cases, e.g., when training a GPLVM, derivatives for equal kernel inputs $\mathbf{x} = \mathbf{z}$ may not be that relevant because different latent points rarely become that close. However, these derivatives are essential for computing the Jacobian covariance matrix (20). Although symbolic differentiation libraries could provide a solution, they tend to be too slow for practical purposes. Therefore, the next best approach is to compute the necessary derivatives and their analytical limits manually. The latter are then used when the inputs \mathbf{x}, \mathbf{z} are closer than a predefined threshold.

Finally, we need the third-order kernel derivatives to optimize pullback geodesics as in the 2D case. We denote the second kernel derivative as $\mathbf{K} = \frac{\partial^2}{\partial \mathbf{z} \partial \mathbf{x}} k(\mathbf{x}, \mathbf{z}) \in \mathbb{R}^{4 \times 4}$. The third-order derivatives can then be obtained by stacking the individual derivatives of each row and column of \mathbf{K} . The derivative of each row \mathbf{K}_i w.r.t. the first input \mathbf{x} and each column \mathbf{K}_j w.r.t. the second input \mathbf{z} are given by,

$$\frac{\partial \mathbf{K}_i}{\partial \mathbf{x}} = \left(q(u) \mathbf{G}^{\mathcal{L}} \mathbf{z} \mathbf{x}^{\top} \mathbf{G}^{\mathcal{L}} z_i + h(u) \mathbf{G}^{\mathcal{L}} z_i + h(u) \mathbf{G}^{\mathcal{L}} \mathbf{z} e_i^{\top} \right) \Delta_{1i} e^{-\frac{\rho^2}{s}},$$

$$\frac{\partial \mathbf{K}_j}{\partial \mathbf{z}} = \left(q(u) \mathbf{G}^{\mathcal{L}} \mathbf{z} \mathbf{x}^{\top} \mathbf{G}^{\mathcal{L}} x_j + h(u) \mathbf{G}^{\mathcal{L}} x_j + h(u) e_j \mathbf{x}^{\top} \mathbf{G}^{\mathcal{L}} \right) \Delta_{1j} e^{-\frac{\rho^2}{s}},$$

where $q(u) = \frac{d}{du} h(u) + \frac{h(u)2\rho}{\nu s}$ and Δ_{ij} represents a modified Kronecker delta equal to -1 for equal indices and to 1 otherwise. Stacking the row and column matrices \mathbf{K}_i and \mathbf{K}_j along the first and second dimension accordingly gives the third kernel derivatives $\frac{\partial}{\partial \mathbf{x}} \mathbf{K}, \frac{\partial}{\partial \mathbf{z}} \mathbf{K} \in \mathbb{R}^{4 \times 4 \times 4}$. Complete derivations are provided in App. B.

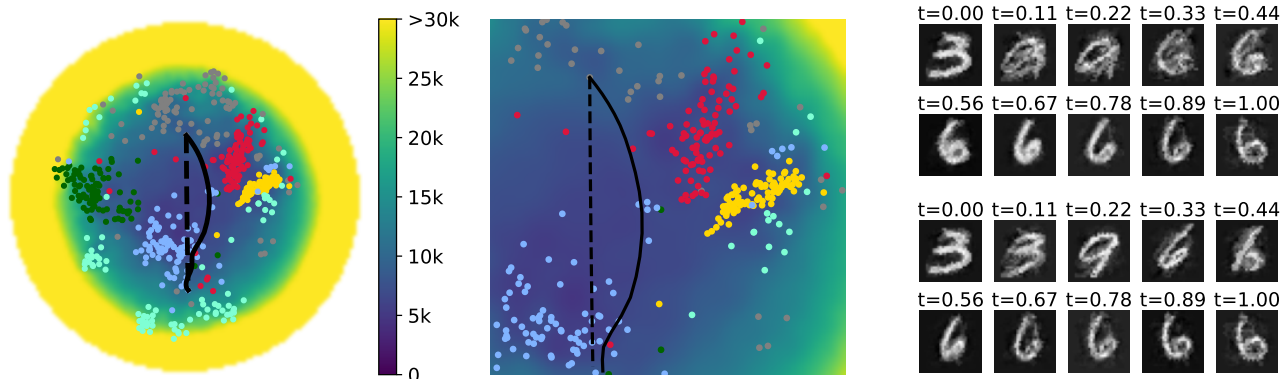


Figure 3: *Left*: Latent embeddings in \mathbb{H}_2^2 of a subset of the MNIST dataset with 0 (●), 1 (●), 2 (●), 3 (●), 6 (●), and 9 (●). The hyperbolic (---) and pullback (—) geodesics interpolate between a 3 and a 6. *Middle*: Zoomed-in view to better visualize the metric volume. *Right*: Ten samples along the decoded geodesics in the image space, corresponding to the hyperbolic (top) and pullback (bottom) geodesic.

5. Experiments

We test the proposed pullback metric in four distinct experiments to demonstrate that (1) the hyperbolic pullback metric augments the hyperbolic metric with the distortions introduced by the GPLVM’s nonlinear mapping; and (2) the hyperbolic pullback geodesics adhere to the data distribution, leading to low uncertainty model predictions. Additional experimental details are provided in App. D.

5.1. C-shape

The first experiment serves as a proof of concept to visualize and compare the Euclidean pullback metric $\mathcal{G}^{\mathbb{P},\mathbb{R}}$ from a GPLVM and the hyperbolic pullback metric $\mathcal{G}^{\mathbb{P},\mathcal{L}}$ from a GPLVM. We use a dataset of N 2D C-shape points as both latent variables and observations. In the hyperbolic case, the latent variables and observations are encoded in the Lorentz model, i.e. $\mathbf{x}, \mathbf{y} \in \mathbb{H}_2^2$, but visualized in the Poincaré model which provides a more intuitive representation. We fully specify the LVMs by setting the variance, length scale, and noise variance as $(\tau, \kappa, \sigma_y^2) = (0.7, 0.15, 0.69)$.

Fig. 2 displays the Euclidean and hyperbolic pullback metric volumes $\sqrt{\det(\mathcal{G}^{\mathbb{P},\mathbb{R}})}$ and $\sqrt{\det(\mathcal{G}^{\mathbb{P},\mathcal{L}})}$. In the hyperbolic case, the pullback metric is a 3×3 matrix lying in the 2D tangent space $\mathcal{T}_{\mathbf{x}^*} \mathbb{H}_2^2$. Therefore, one of its eigenvalues is always zero, which we exclude to effectively visualize the volume. As shown in Fig. 2-*left*, the Euclidean pullback metric volume is small near the C-shape data and increases away from it, until a maximum value is reached. The hyperbolic pullback metric volume is also low nearby the data and additionally follows the hyperbolic geometry: It is low near the origin and increases when moving outwards until it becomes infinite at the boundary of the unit circle (see Fig. 2-*middle*). Overall, the hyperbolic pullback metric effectively integrates the properties of the hyperbolic manifold with those of the data manifold.

Fig. 2 also depicts geodesics generated with and without the pullback metric on both latent manifolds. In both cases, the pullback geodesic closely adheres to the training data. However, in the hyperbolic case, crossing the center experiences a much lower penalty, in terms of curve energy, than in the Euclidean case. Fig. 2-*right* display the curve energy (23) along the geodesics. We observe that the base manifold geodesics and the pullback geodesics both exhibit constant energy, confirming that the optimized curves are true geodesics on their respective manifolds. For comparison, we also show the curve energy of the base manifold geodesic, but evaluated using the pullback metric tensor. Its varying energy indicates that the base manifold geodesic is not a true geodesic with respect to the pullback metric.

5.2. MNIST Digits

The natural clustering of MNIST images can be viewed as a hierarchy whose nodes are each of the 10 digit classes. Following this point of view, Mathieu et al. (2019) showed that hyperbolic LVMs are better suited than their Euclidean counterparts for embedding MNIST images. Similarly to previous works (Arvanitidis et al., 2018; Jørgensen & Hauberg, 2021; Lalchand et al., 2022), we here explore the interpolation of handwritten digits from a subset of the MNIST dataset. We embedded the vectorized 28×28 images in \mathbb{H}_2^2 via a GPLVM and then use the induced pullback metric.

Fig. 3 shows the learned hyperbolic latent space along with two geodesics interpolating between a digit 3 and a digit 6. The decoded hyperbolic geodesic and pullback geodesic, sampled at 10 time steps, show the result of geodesic interpolation in the image space. As expected, the GPLVM predictions collapse to the non-informative GP mean in regions with sparse data, resulting in blurry images. This is particularly evident along the hyperbolic geodesic, in the first half of the trajectory ($t = [0.11, 0.44]$). In contrast, the pullback geodesic tends to avoid empty regions by bending towards

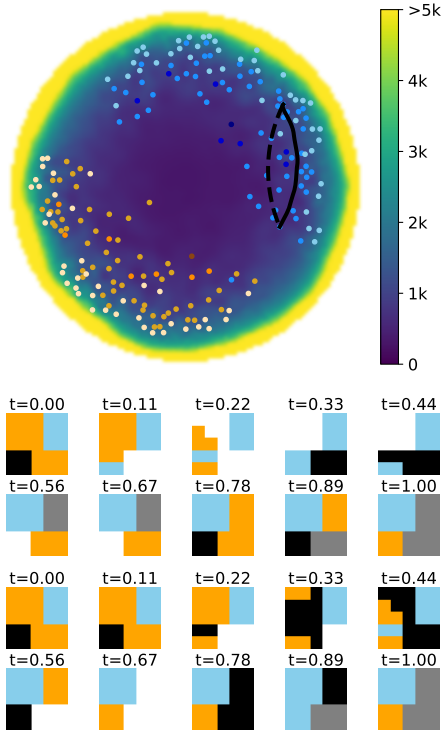


Figure 4: *Top*: Embeddings of multicellular robots from coarse (darker tone) to fine (lighter tone) in \mathbb{H}_P^2 . The embeddings form two clusters originating from an all-vertically-actuated robot (\bullet) and an all-horizontally-actuated robot (\circ). *Bottom*: Ten samples along the decoded hyperbolic (---) and pullback (—) geodesic.

the red cluster (digit 9), leading to less blurry predictions overall. This shows that the pullback metric better captures the data manifold geometry, and thus may be used, e.g., to measure manifold-aware latent distances and probabilities.

5.3. Multi-cellular Robot Design

We build the coarse-to-fine framework for designing multicellular robots using hyperbolic embeddings introduced by Dong et al. (2024). Each robot is composed of a 5×5 grid of cells, where each cell can be horizontally actuated (orange), vertically actuated (blue), rigid (black), soft (gray), or empty (white). The design process begins with a fully horizontally or vertically actuated robot and incrementally introduces changes, forming a hierarchical structure that refines from coarse to fine architectures. This hierarchy can then be queried to find suitable robots for specific tasks. Dong et al. (2024) showed that their multicellular robot design approach in hyperbolic space outperformed its Euclidean counterpart in most of the considered design tasks.

The main goal of this experiment is to leverage pullback geodesics as a data augmentation mechanism, so that we can design new robot architectures by decoding geodesics that follow the pattern of previously-designed robots. To do so, we compute the pullback metric from the hierarchical

Table 2: Average stress and prediction uncertainty (along decoded geodesics). The stress is compared across geometries for each latent space dimension. The prediction uncertainty is compared between the base manifold and pullback geodesic for each model.

MODEL	STRESS ↓	PREDICTION UNCERTAINTY ↓	
		BASE MANIFOLD	PULLBACK
GPLVM \mathbb{R}^2	0.18 ± 0.47	0.0524 ± 0.0199	0.0004 ± 0.0002
GPHLVM \mathbb{H}_C^2	0.10 ± 0.26	0.0150 ± 0.0227	0.0004 ± 0.0002
GPLVM \mathbb{R}^3	0.11 ± 0.21	0.0030 ± 0.0036	0.0001 ± 0.0001
GPHLVM \mathbb{H}_C^3	0.07 ± 0.10	0.0129 ± 0.0150	0.0003 ± 0.0003

multicellular robot embeddings and optimize geodesics to interpolate between existing robot designs, generating novel ones. Fig. 4 shows the latent space and the mean predictions along both the hyperbolic and pullback geodesics. Note that, while the hyperbolic geodesic produces invalid robot designs, e.g., separated sections at $t = 0.22$, the pullback geodesic avoids this issue by complying with the geometry of the data support. This experiment suggests that pullback geodesics can assist the robot design process.

5.4. Hand Grasps Generation

Jaquier et al. (2024) showed that GPHLVM outperform Euclidean GPLVM to learn hand grasp embeddings that comply with the hierarchical structure of human motion taxonomies. Here, we build on this model and explore the use of pullback geodesics as a motion generation mechanism with the aim of creating new motions that transition from one grasp to another. We consider the hand grasp taxonomy of Stival et al. (2019), which organizes common grasps types within a hierarchical taxonomy tree. We use a dataset from the KIT whole-body motion database (Mandery et al., 2016) consisting of 38 motions of 19 grasp types obtained from recordings of humans grasping different objects. Each motion corresponds to a subject reaching out to grasp an object from an initial resting pose and results in a trajectory $\mathbf{Y} \in \mathbb{R}^{N \times 24}$ representing the temporal evolution of the 24 degrees of freedom of the wrist and fingers.

We train two GPHLVMs augmented with a taxonomy graph-distance prior (Jaquier et al., 2024) and a dynamic prior akin to (Wang et al., 2008) (see App. D.4). Fig. 5 shows the resulting 2D and 3D latent spaces. All training trajectories start near the latent space origin, corresponding to the hand’s initial resting pose, and progress outward until the final grasp. We evaluate the embedding quality via the stress loss ℓ_{stress} , that quantifies the preservation of the taxonomy graph distances by the embeddings (see App. D.4 for details). Next, we compare the GPHLVMs with GPLVMs (see also App. D.5). Table 2 shows that the hyperbolic models better capture the taxonomy structure than their Euclidean counterparts, consistent with (Jaquier et al., 2024).

Fig. 5 shows the hyperbolic and pullback geodesics interpolating from a ring to a spherical grasp, alongside the decoded hand motions. While the hyperbolic geodesic crosses

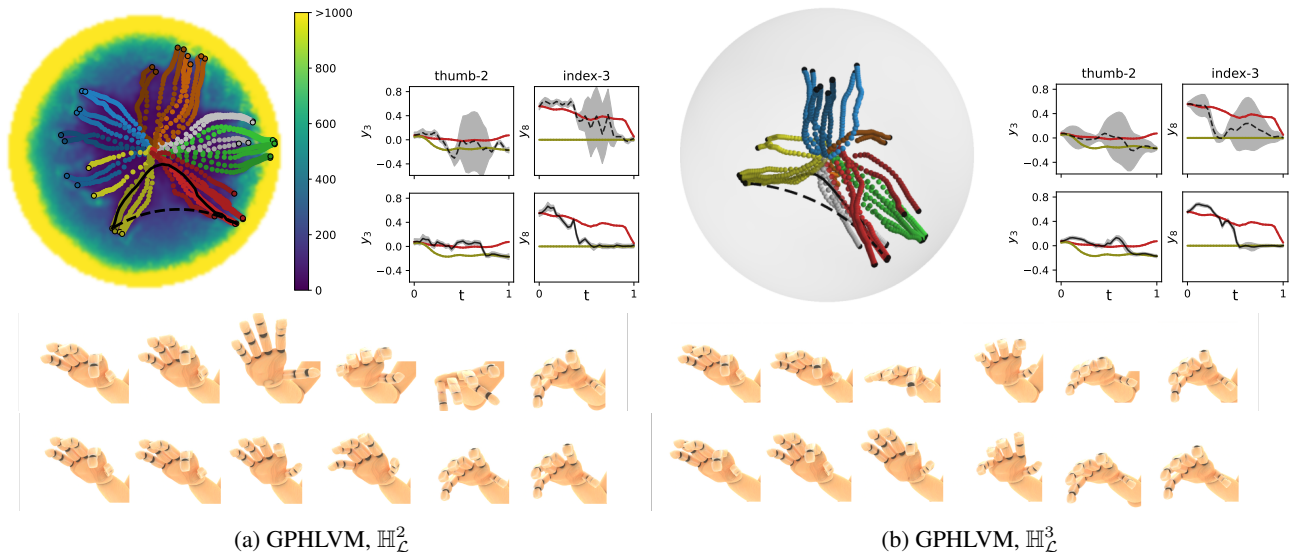


Figure 5: Hand grasps transition from a ring (\bullet) to a spherical grasp (\bullet) using hyperbolic (---) and pullback (—) geodesics in (a) $\mathbb{H}_{\mathcal{L}}^2$ and (b) $\mathbb{H}_{\mathcal{L}}^3$. *Top left*: Latent embeddings. The latent trajectory points are colored according to their corresponding grasp class. The background color in $\mathbb{H}_{\mathcal{L}}^2$ represents the pullback metric volume. *Top right*: Time-series plots of 2 dimensions of the joint space. The top and bottom rows show the mean of the decoded hyperbolic (---) and pullback geodesics (—) with their uncertainty as a gray envelope. A training trajectory to the spherical grasp (—) and a reversed training trajectory from the ring grasp (—) are included for reference. *Bottom*: Generated hand trajectories from the decoded hyperbolic (top) and pullback (bottom) geodesics.

empty regions in the latent space, the pullback geodesic adheres closely to the data support. As both geodesics start and end with the same grasps, their initial and final predictions match. However, the decoded hyperbolic geodesic shows high uncertainty in the middle part of the motion (see Figs. 5a-5b top right). This is due to the GP reverting to its non-informative mean in regions with no data, where the GP prior dominates the posterior, leading to maximum uncertainty. Consequently, the obtained hand motions display large deviations from the initial ring and final spherical grasps. In contrast, as shown in Fig. 5 and Table 2, the decoded pullback geodesic shows much lower uncertainty, as the geodesic stays closer to the data support. Note that this mirrors the behavior of the GPLVM Euclidean pullback geodesics compared to straight lines (see Fig. 8 in App. D.5 and Table 2), thus highlighting the successful adaptation of the pullback approach to hyperbolic spaces. Moreover, the hand motions obtained from the decoded pullback geodesics result in more realistic transitions that those obtained with the hyperbolic ones. Despite the low uncertainty, the predicted motions sometimes lack smoothness due to the fact that nearby latent points do not always correspond to equally similar hand configurations (i.e., similar joint values). This is mostly alleviated in the 3D latent space, which provides more room to accommodate the latent embeddings.

6. Conclusion

This paper advances the field of hyperbolic LVMs by augmenting the hyperbolic manifold with a Riemannian pull-

back metric that combines the hyperbolic geometry with the geometry of the data distribution. By minimizing the curve energy on the pullback metric, we computed geodesics that adhere to the data manifold in the hyperbolic latent space. To do so, we addressed the limitations of current auto-differentiation techniques by providing analytical solutions for the hyperbolic SE kernel derivatives. Via multiple experiments, we demonstrated that pullback geodesics outperform standard hyperbolic geodesics.

It is worth noting that the benefits of pullback geodesics are most evident when the data exhibits smooth transitions. They become less effective when the data is inherently comprised of distinct clusters, as the pullback geodesics cannot cross high-energy regions, i.e., the data manifold boundaries. This paper focused on 2D and 3D hyperbolic latent spaces as they are easier to visualize and computationally less expensive than higher-dimensional latent spaces, while benefiting from the increased capacity of hyperbolic spaces to embed hierarchical data. Future work will investigate extensions to higher-dimensional hyperbolic latent spaces, which require to deal with more complex expressions for hyperbolic kernels. Additionally, the need for computing manual kernel derivatives is unsatisfactory. Future work will explore alternative autodifferentiation techniques built on KeOps (Feydy et al., 2020) to overcome this practical issue. Finally, the approximation of the 2D hyperbolic SE kernel is computationally expensive. Performance could potentially be increased by exploring different sampling strategies, e.g., by sampling from a Rayleigh distribution rather than from a Gaussian.

Acknowledgements

This work was partially supported by the Carl Zeiss Foundation under the project JuBot, by the European Union’s Horizon Europe Framework Programme under grant agreement No 101070596 (euROBIN), and by the Wallenberg AI, Autonomous Systems and Software Program (WASP) funded by the Knut and Alice Wallenberg Foundation.

References

- Alanis-Lobato, G., Mier, P., and Andrade-Navarro, M. The latent geometry of the human protein interaction network. *Bioinformatics*, 34(16):2826–2834, 2018. URL <https://doi.org/10.1093/bioinformatics/bty206>.
- Anderson, T. The non-central wishart distribution and certain problems of multivariate statistics. *The Annals of Mathematical Statistics*, 17(4):409–431, 1946. URL <https://www.jstor.org/stable/pdf/2236082.pdf>.
- Arvanitidis, G., Hansen, L. K., and Hauberg, S. Latent space oddity: on the curvature of deep generative models. In *Intl. Conf. on Learning Representations (ICLR)*, 2018. URL <https://openreview.net/forum?id=SJzRZ-WCZ>.
- Arvanitidis, G., Hauberg, S., and Schölkopf, B. Geometrically enriched latent spaces. In *Intl. Conf. on Artificial Intelligence and Statistics (AISTATS)*, 2021. URL <https://proceedings.mlr.press/v130/arvanitidis21a.html>.
- Beik-Mohammadi, H., Hauberg, S., Arvanitidis, G., Neumann, G., and Rozo, L. Learning Riemannian manifolds for geodesic motion skills. In *Robotics: Science and Systems (R:SS)*, 2021. URL <https://arxiv.org/abs/2106.04315>.
- Bishop, C. *Pattern Recognition and Machine Learning*. Springer, January 2006. URL <https://www.microsoft.com/en-us/research/publication/pattern-recognition-machine-learning/>.
- Borovitskiy, V., Terenin, A., Mostowsky, P., and Deisenroth, M. P. Matérn Gaussian processes on Riemannian manifolds. In *Neural Information Processing Systems (NeurIPS)*, pp. 12426–12437, 2020. URL <https://proceedings.neurips.cc/paper/2020/file/92bf5e6240737e0326ea59846a83e076-Paper.pdf>.
- Borovitskiy, V., Azangulov, I., Terenin, A., Mostowsky, P., Deisenroth, M., and Durrande, N. Matérn Gaussian processes on graphs. In *Intl. Conf. on Artificial Intelligence and Statistics (AISTATS)*, pp. 2593–2601, 2021. URL <https://proceedings.mlr.press/v130/borovitskiy21a.html>.
- Boumal, N. *An introduction to optimization on smooth manifolds*. Cambridge University Press, 2023. URL <http://www.nicolasboumal.net/book>.
- Bécigneul, G. and Ganea, O.-E. Riemannian adaptive optimization methods. In *International Conference on Learning Representations (ICLR)*, 2019. URL <https://openreview.net/pdf?id=rleiqi09K7>.
- Chadebec, C., Thibeau-Sutre, E., Burgos, N., and Allas-sonnière, S. Data augmentation in high dimensional low sample size setting using a geometry-based variational autoencoder. *IEEE Transactions on Pattern Analysis and Machine Intelligence*, 45(3):2879–2896, 2023. doi: 10.1109/TPAMI.2022.3185773.
- Cho, S., Lee, J., and Kim, D. Hyperbolic VAE via latent gaussian distributions. In *Neural Information Processing Systems (NeurIPS)*, 2023. URL <https://openreview.net/forum?id=FNn4zibGvw>.
- Cvetkovski, A. and Crovella, M. Hyperbolic embedding and routing for dynamic graphs. In *IEEE INFOCOM 2009*, pp. 1647–1655, 2009. doi: 10.1109/INFCOM.2009.5062083.
- Detlefsen, N. S., Hauberg, S., and Boomsma, W. Learning meaningful representations of protein sequences. *Nature Communications*, 13(1):1914, 2022. URL <https://doi.org/10.1038/s41467-022-29443-w>.
- Dong, H., Zhang, J., and Zhang, C. Leveraging hyperbolic embeddings for coarse-to-fine robot design. In *Intl. Conf. on Learning Representations (ICLR)*, 2024. URL <https://openreview.net/forum?id=q9jQPA6zPK>.
- Doorenbos, L., Neila, P. M., Sznitman, R., and Mettes, P. Hyperbolic random forests. *Transactions on Machine Learning Research*, 2024. ISSN 2835-8856. URL <https://openreview.net/forum?id=pjKcIzvXWR>.
- Feix, T., Romero, J., Schmiedmayer, H.-B., Dollar, A. M., and Kragic, D. The GRASP taxonomy of human grasp types. *IEEE Transactions on Human-Machine Systems*, 46(1):66–77, 2016. doi: 10.1109/THMS.2015.2470657.
- Feydy, J., Glaunès, J., Charlier, B., and Bronstein, M. Fast geometric learning with symbolic matrices. In *Neural Information Processing Systems (NeurIPS)*, volume 33, 2020.

- Gousenbourger, P.-Y., Samir, C., and Absil, P. Piecewise-bézier c1 interpolation on riemannian manifolds with application to 2d shape morphing. In *Intl. Conf. on Pattern Recognition*, pp. 4086–4091, 2014.
- Grigoryan, A. and Noguchi, M. The heat kernel on hyperbolic space. *Bulletin of the London Mathematical Society*, 30(6):643–650, 1998. doi: 10.1112/S0024609398004780.
- Hauberg, S. Only Bayes should learn a manifold. *arXiv preprint arXiv:1806.04994*, 2019. URL <https://arxiv.org/abs/1806.04994>.
- Heeren, B., Rumpf, M., and Wirth, B. Variational time discretization of Riemannian splines. *IMA Journal of Numerical Analysis*, 39(1):61–104, 2018. doi: 10.1093/imanum/drx077.
- Jansen, H. Abbildung der hyperbolischen geometrie auf ein zweischaliges hyperboloid. *Mitteilungen der Mathematischen Gesellschaft in Hamburg*, 4:409–440, 1909.
- Jaquier, N., Borovitskiy, V., Smolensky, A., Terenin, A., Asfour, T., and Rozo, L. Geometry-aware Bayesian optimization in robotics using Riemannian Matérn kernels. In *Conference on Robot Learning (CoRL)*, 2021. URL <https://openreview.net/forum?id=ovRdr3FOIIm>.
- Jaquier, N., Rozo, L., González-Duque, M., Borovitskiy, V., and Asfour, T. Bringing motion taxonomies to continuous domains via GPLVM on hyperbolic manifolds. In *International Conference on Machine Learning (ICML)*, 2024.
- Jørgensen, M. and Hauberg, S. Isometric Gaussian process latent variable model for dissimilarity data. In *Intl. Conf. on Machine Learning (ICML)*, pp. 5127–5136, 2021. URL <https://proceedings.mlr.press/v139/jorgensen21a.html>.
- Khrulkov, V., Mirvakhobova, L., Ustinova, E., Oseledets, I., and Lempitsky, V. Hyperbolic image embeddings. In *Conf. on Computer Vision and Pattern Recognition (CVPR)*, 2020. URL <https://arxiv.org/abs/1904.02239>.
- Kolda, T. G. and Bader, B. W. Tensor decompositions and applications. *SIAM Review*, 51(3):455–500, 2009a. doi: 10.1137/07070111x.
- Kolda, T. G. and Bader, B. W. Tensor Decompositions and Applications. *SIAM Review*, 51(3):455–500, 2009b. doi: 10.1137/07070111x.
- Krioukov, D., Papadopoulos, F., Kitsak, M., Vahdat, A., and Boguñá, M. Hyperbolic geometry of complex networks. *Phys. Rev. E*, 82:036106, 2010. URL <https://link.aps.org/doi/10.1103/PhysRevE.82.036106>.
- Lalchand, V., Ravuri, A., and Lawrence, N. D. Generalised GPLVM with stochastic variational inference. In *Intl. Conf. on Artificial Intelligence and Statistics (AISTATS)*, pp. 7841–7864, 2022. URL <https://proceedings.mlr.press/v151/lalchand22a.html>.
- Lawrence, N. D. Gaussian process latent variable models for visualisation of high dimensional data. In *Neural Information Processing Systems (NeurIPS)*, 2003. URL <https://proceedings.neurips.cc/paper/2003/file/9657c1ffffd38824e5ab0472e022e577e-Paper.pdf>.
- Lee, J. *Introduction to Riemannian Manifolds*. Springer, 2nd edition, 2018. doi: 10.1007/978-3-319-91755-9.
- Lin, Y.-W. E., Coifman, R. R., Mishne, G., and Talmon, R. Hyperbolic diffusion embedding and distance for hierarchical representation learning. In *Intl. Conf. on Machine Learning (ICML)*, pp. 21003–21025, 2023. URL <https://proceedings.mlr.press/v202/lin23b.html>.
- Mandery, C., Terlemez, O., Do, M., Vahrenkamp, N., and Asfour, T. Unifying representations and large-scale whole-body motion databases for studying human motion. *IEEE Trans. on Robotics*, 32(4):796–809, 2016. doi: 10.1109/TRO.2016.2572685.
- Mathieu, E., Le Lan, C., Maddison, C. J., Tomioka, R., and Teh, Y. W. Continuous hierarchical representations with Poincaré variational auto-encoders. In *Neural Information Processing Systems (NeurIPS)*, 2019. URL <https://proceedings.neurips.cc/paper/2019/file/0ec04cb3912c4f08874dd03716f80df1-Paper.pdf>.
- Nagano, Y., Yamaguchi, S., Fujita, Y., and Koyama, M. A wrapped normal distribution on hyperbolic space for gradient-based learning. In *Intl. Conf. on Machine Learning (ICML)*, pp. 4693–4702, 2019. URL <https://proceedings.mlr.press/v97/nagano19a.html>.
- Nickel, M. and Kiela, D. Poincaré embeddings for learning hierarchical representations. In *Neural Information Processing Systems (NeurIPS)*, 2017. URL <https://arxiv.org/abs/1705.08039>.
- Nickel, M. and Kiela, D. Learning continuous hierarchies in the Lorentz model of hyperbolic geometry. In *Intl.*

- Conf. on Machine Learning (ICML)*, pp. 3779–3788, 2018. URL <http://proceedings.mlr.press/v80/nickell18a.html>.
- Paszke, A., Gross, S., Massa, F., Lerer, A., Bradbury, J., Chanan, G., Killeen, T., Lin, Z., Gimelshein, N., Antiga, L., Desmaison, A., Köpf, A., Yang, E., DeVito, Z., Raison, M., Tejani, A., Chilamkurthy, S., Steiner, B., Fang, L., Bai, J., and Chintala, S. Pytorch: an imperative style, high-performance deep learning library. In *Neural Information Processing Systems (NeurIPS)*, 2019. URL https://proceedings.neurips.cc/paper_files/paper/2019/file/bdbca288fee7f92f2bfa9f7012727740-Paper.pdf.
- Poincaré, H. Théorie des groupes fuchsien. *Acta Mathematica*, 1:1–62, 1900. URL <https://doi.org/10.1007/BF02592124>.
- Rasmussen, C. E. and Williams, C. K. *Gaussian Processes for Machine Learning*. MIT Press, 2006. URL <http://www.gaussianprocess.org/gpml/>.
- Ratcliffe, J. G. *Foundations of Hyperbolic Manifolds*. Springer, 3rd edition, 2019. doi: 10.1007/978-3-030-31597-9.
- Reynolds, W. F. Hyperbolic geometry on a hyperboloid. *The American Mathematical Monthly*, 100(5):442–455, 1993. URL <https://doi.org/10.1080/00029890.1993.11990430>.
- Sala, F., De Sa, C., Gu, A., and Re, C. Representation tradeoffs for hyperbolic embeddings. In *Intl. Conf. on Machine Learning (ICML)*, pp. 4460–4469, 2018. URL <https://proceedings.mlr.press/v80/sala18a.html>.
- Skopek, O., Ganea, O.-E., and Bécigneul, G. Mixed-curvature variational autoencoders. In *Intl. Conf. on Learning Representations (ICLR)*, 2020. URL <https://openreview.net/forum?id=S1g6xeSKDS>.
- Sonthalia, R. and Gilbert, A. Tree! i am no tree! i am a low dimensional hyperbolic embedding. In *Neural Information Processing Systems (NeurIPS)*, volume 33, pp. 845–856, 2020. URL https://proceedings.neurips.cc/paper_files/paper/2020/file/093f65e080a295f8076b1c5722a46aa2-Paper.pdf.
- Stival, F., Michieletto, S., Cognolato, M., Pagello, E., Müller, H., and Atzori, M. A quantitative taxonomy of human hand grasps. *Journal of NeuroEngineering and Rehabilitation*, 16(28), 2019. doi: 10.1186/s12984-019-0488-x.
- Tosi, A., Hauberg, S., Vellido, A., and Lawrence, N. D. Metrics for probabilistic geometries. In *Conference on Uncertainty in Artificial Intelligence (UAI)*, 2014.
- Wang, J. M., Fleet, D. J., and Hertzmann, A. Gaussian process dynamical models for human motion. *IEEE Transactions on Pattern Analysis and Machine Intelligence*, 30(2):283–298, 2008. doi: 10.1109/TPAMI.2007.1167.
- Yang, M., Zhou, M., Ying, R., Chen, Y., and King, I. Hyperbolic representation learning: Revisiting and advancing. In *Intl. Conf. on Machine Learning (ICML)*, pp. 39639–39659, 2023. URL <https://proceedings.mlr.press/v202/yang23u.html>.

A. Hyperbolic Manifold

The D -dimensional hyperbolic manifold $\mathbb{H}_{\mathcal{L}}^D$ and its tangent space $\mathcal{T}_{\mathbf{x}}\mathbb{H}_{\mathcal{L}}^D$ are given as

$$\mathbb{H}_{\mathcal{L}}^D = \{\mathbf{x} \in \mathbb{R}^{D+1} \mid \langle \mathbf{x}, \mathbf{x} \rangle_{\mathcal{L}} = -1, x_0 > 0\}, \quad (31)$$

$$\mathcal{T}_{\mathbf{x}}\mathbb{H}_{\mathcal{L}}^D = \{\mathbf{u} \in \mathbb{R}^{D+1} \mid \langle \mathbf{u}, \mathbf{x} \rangle_{\mathcal{L}} = 0\}, \quad (32)$$

where $\langle \mathbf{x}, \mathbf{y} \rangle_{\mathcal{L}} = \mathbf{x}^{\top} \mathbf{G}^{\mathcal{L}} \mathbf{y}$ is the Lorentzian inner product with the Lorentzian metric tensor $\mathbf{G}^{\mathcal{L}} = \text{diag}(-1, 1, \dots, 1)$. Note that, since the curvature of the hyperbolic manifold is constant, the metric tensor does not depend on \mathbf{x} as for general manifolds, i.e., $\mathbf{G}_{\mathbf{x}}^{\mathcal{L}} = \mathbf{G}^{\mathcal{L}}$ for all $\mathbf{x} \in \mathbb{H}_{\mathcal{L}}^D$. For the hyperbolic manifold, closed form solutions exist for the standard manifold operations. Specifically, the geodesic distance, exponential map, logarithmic map, parallel transport, and tangent space projection are given as,

$$d_{\mathbb{H}_{\mathcal{L}}^D}(\mathbf{x}, \mathbf{y}) = \text{arccosh}(-\langle \mathbf{x}, \mathbf{y} \rangle_{\mathcal{L}}), \quad (33)$$

$$\text{Exp}_{\mathbf{x}}(\mathbf{u}) = \cosh(\|\mathbf{u}\|_{\mathcal{L}})\mathbf{x} + \sinh(\|\mathbf{u}\|_{\mathcal{L}}) \frac{\mathbf{u}}{\|\mathbf{u}\|_{\mathcal{L}}}, \quad (34)$$

$$\text{Log}_{\mathbf{x}}(\mathbf{y}) = d_{\mathbb{H}_{\mathcal{L}}^D}(\mathbf{x}, \mathbf{y}) \frac{\mathbf{y} + \langle \mathbf{x}, \mathbf{y} \rangle_{\mathcal{L}} \mathbf{x}}{\sqrt{\langle \mathbf{x}, \mathbf{y} \rangle_{\mathcal{L}}^2 - 1}}, \quad (35)$$

$$\Gamma_{\mathbf{x} \rightarrow \mathbf{y}}(\mathbf{u}) = \mathbf{u} + \frac{\langle \mathbf{y}, \mathbf{u} \rangle_{\mathcal{L}}}{1 - \langle \mathbf{x}, \mathbf{y} \rangle_{\mathcal{L}}} (\mathbf{x} + \mathbf{y}) \quad (36)$$

$$\text{proj}_{\mathbf{x}}(\mathbf{w}) = \mathbf{P}_{\mathbf{x}} \mathbf{w} = (\mathbf{G}^{\mathcal{L}} + \mathbf{x} \mathbf{x}^{\top}) \mathbf{w}. \quad (37)$$

These operations are illustrated by Fig. 6.

Working with probabilistic models on Riemannian manifolds requires probability distributions that account for their geometry. Therefore, the GPHLVM prior $x_n \sim \mathcal{N}_{\mathbb{H}_{\mathcal{L}}^D}(\boldsymbol{\mu}_0, \alpha \mathbf{I})$ relies on the hyperbolic wrapped distribution (Nagano et al., 2019), which builds on a Gaussian distribution on the tangent space at the origin $\boldsymbol{\mu}_0 = [1 \ 0 \ \dots \ 0]^{\top} \in \mathbb{H}_{\mathcal{L}}^D$. Intuitively, the wrapped distribution is constructed as follows: (1) Sample a point $\tilde{\mathbf{v}} \in \mathbb{R}^D$ from the Euclidean Gaussian distribution $\mathcal{N}(\mathbf{0}, \boldsymbol{\Sigma})$; (2) Transform $\tilde{\mathbf{v}}$ to an element of the tangent space $\mathcal{T}_{\boldsymbol{\mu}_0}\mathbb{H}_{\mathcal{L}}^D$ at the origin by setting $\mathbf{v} = [0 \ \tilde{\mathbf{v}}]^{\top}$; (3) Parallel transport \mathbf{v} to the desired mean $\mathbf{u} = \Gamma_{\boldsymbol{\mu}_0 \rightarrow \boldsymbol{\mu}}(\mathbf{v})$; and (4) Project \mathbf{u} onto the hyperbolic space via the exponential map $\mathbf{x} = \text{Exp}_{\boldsymbol{\mu}}(\mathbf{u})$. The resulting probability density function is

$$\mathcal{N}_{\mathbb{H}_{\mathcal{L}}^D}(\mathbf{x} \mid \boldsymbol{\mu}, \boldsymbol{\Sigma}) = \mathcal{N}(\tilde{\mathbf{v}} \mid \mathbf{0}, \boldsymbol{\Sigma}) \left(\frac{r}{\sinh(r)} \right)^{D-1}, \quad (38)$$

where $\mathbf{u} = \text{Log}_{\boldsymbol{\mu}}(\mathbf{x})$, $\mathbf{v} = \Gamma_{\boldsymbol{\mu} \rightarrow \boldsymbol{\mu}_0}(\mathbf{u})$, and $r = \|\mathbf{u}\|_{\mathcal{L}}$.

As mentioned in the main text, we mostly rely on the Lorentz model $\mathbb{H}_{\mathcal{L}}^D$ in our algorithms, but use the Poincaré model for visualization, as it provides a more intuitive representation. The Poincaré model is defined as

$$\mathbb{H}_{\mathcal{P}}^D = \{\mathbf{x}_{\mathcal{P}} \in \mathbb{R}^D \mid \|\mathbf{x}_{\mathcal{P}}\| < 1\}. \quad (39)$$

It is possible to map points from the Lorentz to the Poincaré model via an isometric mapping $f : \mathbb{H}_{\mathcal{L}}^D \rightarrow \mathbb{H}_{\mathcal{P}}^D$ such that

$$f(\mathbf{x}) = \frac{(x_1, \dots, x_d)^{\top}}{x_0 + 1}, \quad (40)$$

where $\mathbf{x} \in \mathbb{H}_{\mathcal{L}}^D$ with components x_0, x_1, \dots, x_d . The inverse mapping $f^{-1} : \mathbb{H}_{\mathcal{P}}^D \rightarrow \mathbb{H}_{\mathcal{L}}^D$ is defined as follows

$$f^{-1}(\mathbf{y}) = \frac{(1 + \|\mathbf{y}\|^2, 2y_1, \dots, 2y_d)^{\top}}{1 - \|\mathbf{y}\|^2}, \quad (41)$$

with $\mathbf{y} \in \mathbb{H}_{\mathcal{P}}^D$ with components y_1, \dots, y_d .

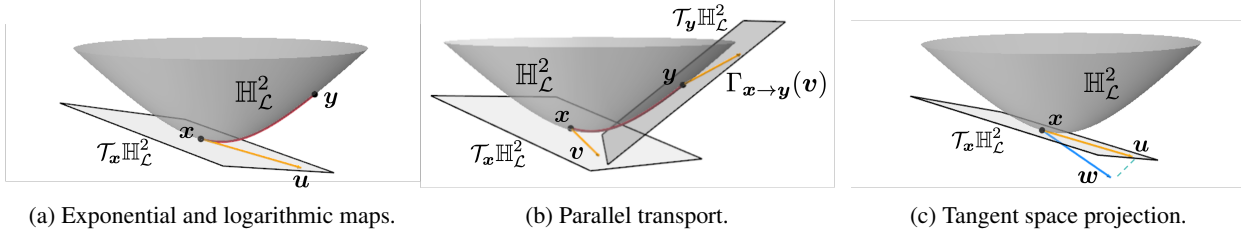


Figure 6: Principal Riemannian operations on the Lorentz model $\mathbb{H}_{\mathcal{L}}^2$. **(a)** The geodesic (—) is the shortest path between the two points x to y on the manifold. Its length is equal to the geodesic distance $d_{\mathbb{H}_{\mathcal{L}}^2}(x, y)$. The vector u (—) lies on the tangent space of x such that $y = \text{Exp}_x(u)$. **(b)** Parallel transport $\Gamma_{x \rightarrow y}(v)$ of the vector v from $\mathcal{T}_x \mathbb{H}_{\mathcal{L}}^2$ to $\mathcal{T}_y \mathbb{H}_{\mathcal{L}}^2$. **(c)** The vector w (—) is projected onto the tangent space of x via the tangent space projection $u = \text{proj}_x(w)$.

B. Hyperbolic Kernel Derivatives

This section provides the complete derivations of the hyperbolic SE kernel derivatives that are necessary to compute the pullback metric tensor and to optimize geodesics on it. Eq. (22) defines the pullback metric tensor $\mathbf{G}_{\mathbf{x}^*}^{\mathbf{P}, \mathcal{L}}$ based on the Jacobian mean $\boldsymbol{\mu}_J$ (19) and covariance matrix $\boldsymbol{\Sigma}_J$ (20), which in turn require the kernel derivatives $\partial k(\mathbf{x}^*, \mathbf{X}) = \frac{\partial}{\partial \mathbf{x}^*} k(\mathbf{x}^*, \mathbf{X}) \in \mathbb{R}^{D_x \times N}$ and $\partial^2 k(\mathbf{x}^*, \mathbf{x}^*) = \frac{\partial^2}{\partial z^2 \partial \mathbf{x}} k(\mathbf{x}, z)|_{\mathbf{x}=z=\mathbf{x}^*} \in \mathbb{R}^{D_x \times D_x}$. Additionally, minimizing the curve energy (23), requires the derivative of the pullback metric tensor, i.e., the derivative of $\boldsymbol{\mu}_J^\top \boldsymbol{\mu}_J + D_y \boldsymbol{\Sigma}_J$, which requires the kernel derivative $\frac{\partial^3}{\partial \mathbf{x} \partial z \partial \mathbf{x}} k(\mathbf{x}, z)$ and $\frac{\partial^3}{\partial z^2 \partial \mathbf{x}} k(\mathbf{x}, z)$. Specifically, we have

$$\frac{\partial}{\partial \mathbf{x}^*} (\boldsymbol{\mu}_J^\top \boldsymbol{\mu}_J + D_y \boldsymbol{\Sigma}_J) = \left[\frac{\partial}{\partial \mathbf{x}^*} \boldsymbol{\mu}_J^\top \right] \times_2 \boldsymbol{\mu}_J^\top + \left[\frac{\partial}{\partial \mathbf{x}^*} \boldsymbol{\mu}_J \right] \times_1 \boldsymbol{\mu}_J^\top + D_y \left[\frac{\partial}{\partial \mathbf{x}^*} \boldsymbol{\Sigma}_J \right], \quad (42)$$

$$\text{with } \frac{\partial}{\partial \mathbf{x}^*} \boldsymbol{\mu}_J^\top = \left[\frac{\partial}{\partial \mathbf{x}^*} \partial k(\mathbf{x}^*, \mathbf{X}) \right] \times_2 \mathbf{Y}^\top (\mathbf{K}_X + \sigma_y^2 \mathbf{I}_N)^{-1}, \quad (43)$$

$$\frac{\partial}{\partial \mathbf{x}^*} \boldsymbol{\Sigma}_J = \left[\frac{\partial}{\partial \mathbf{x}^*} \partial^2 k(\mathbf{x}^*, \mathbf{x}^*) \right] - \left[\frac{\partial}{\partial \mathbf{x}^*} \partial k(\mathbf{x}^*, \mathbf{X}) \right] \times_2 \mathbf{S}_J - \left[\frac{\partial}{\partial \mathbf{x}^*} \partial k(\mathbf{X}, \mathbf{x}^*) \right] \times_1 \mathbf{S}_J, \quad (44)$$

$$\frac{\partial}{\partial \mathbf{x}^*} \partial^2 k(\mathbf{x}^*, \mathbf{x}^*) = \left[\frac{\partial^3}{\partial \mathbf{x} \partial z \partial \mathbf{x}} k(\mathbf{x}, z) + \frac{\partial^3}{\partial z^2 \partial \mathbf{x}} k(\mathbf{x}, z) \right] \Bigg|_{\mathbf{x}=z=\mathbf{x}^*}, \quad (45)$$

where we have $\boldsymbol{\mu}_J \in \mathbb{R}^{D_y \times D_x}$, $\frac{\partial}{\partial \mathbf{x}^*} \boldsymbol{\mu} \in \mathbb{R}^{D_y \times D_x \times D_x}$, $\frac{\partial}{\partial \mathbf{x}^*} \partial k(\mathbf{x}^*, \mathbf{X}) \in \mathbb{R}^{D_x \times N \times D_x}$, and \times_n denotes the n -th mode tensor product (Kolda & Bader, 2009a). Next, we provide the details of the derivation of the kernel derivatives for $\mathbb{H}_{\mathcal{L}}^2$ and $\mathbb{H}_{\mathcal{L}}^3$.

B.1. 2D Hyperbolic SE Kernel Derivatives

As discussed in Sec. 4.1, the derivatives of the 2D hyperbolic SE kernel (6) are entirely determined by the derivatives of $\Phi_l(\mathbf{x}, z)$. Eqs (25), (26), (27), and (28) show that these derivatives in turn are defined by the first and second derivatives of

$\phi_l(\mathbf{x}_P) = e^{(1+2s_l i)\langle \mathbf{x}_P, \mathbf{b}_l \rangle}$, which are computed as

$$\frac{\partial}{\partial \mathbf{x}} \phi_l(\mathbf{x}_P) = (1 + 2s_l i) \phi_l(\mathbf{x}_P) \left[\frac{\partial}{\partial \mathbf{x}} \mathbf{x}_P \right]^\top \left[\frac{\partial}{\partial \mathbf{x}_P} \langle \mathbf{x}_P, \mathbf{b} \rangle \right], \quad (46)$$

$$\begin{aligned} \frac{\partial^2}{\partial \mathbf{x}^2} \phi_l(\mathbf{x}_P) &= (1 + 2s_l i) \left(\left[\frac{\partial}{\partial \mathbf{x}} \mathbf{x}_P \right]^\top \left[\frac{\partial}{\partial \mathbf{x}_P} \langle \mathbf{x}_P, \mathbf{b} \rangle \right] \left[\frac{\partial}{\partial \mathbf{x}} \phi_l(\mathbf{x}_P) \right]^\top \right. \\ &\quad + \phi_l(\mathbf{x}_P) \left[\frac{\partial^2}{\partial \mathbf{x}^2} \mathbf{x}_P \right] \times_1 \left[\frac{\partial}{\partial \mathbf{x}_P} \langle \mathbf{x}_P, \mathbf{b} \rangle \right] \\ &\quad \left. + \phi_l(\mathbf{x}_P) \left[\frac{\partial}{\partial \mathbf{x}} \mathbf{x}_P \right]^\top \left[\frac{\partial}{\partial \mathbf{x}} \frac{\partial}{\partial \mathbf{x}_P} \langle \mathbf{x}_P, \mathbf{b} \rangle \right] \right), \end{aligned} \quad (47)$$

$$\begin{aligned} &= (1 + 2s_l i) \phi_l(\mathbf{x}_P) \left((1 + 2s_l i) \left[\frac{\partial}{\partial \mathbf{x}} \mathbf{x}_P \right]^\top \left[\frac{\partial}{\partial \mathbf{x}_P} \langle \mathbf{x}_P, \mathbf{b} \rangle \right] \left[\frac{\partial}{\partial \mathbf{x}_P} \langle \mathbf{x}_P, \mathbf{b} \rangle \right]^\top \left[\frac{\partial}{\partial \mathbf{x}} \mathbf{x}_P \right] \right. \\ &\quad + \left[\frac{\partial^2}{\partial \mathbf{x}^2} \mathbf{x}_P \right] \times_1 \left[\frac{\partial}{\partial \mathbf{x}_P} \langle \mathbf{x}_P, \mathbf{b} \rangle \right] \\ &\quad \left. + \left[\frac{\partial}{\partial \mathbf{x}} \mathbf{x}_P \right]^\top \left[\frac{\partial^2}{\partial \mathbf{x}_P^2} \langle \mathbf{x}_P, \mathbf{b} \rangle \right] \left[\frac{\partial}{\partial \mathbf{x}} \mathbf{x}_P \right] \right). \end{aligned} \quad (48)$$

As shown by these expressions, the derivatives of $\phi_l(\mathbf{x}_P)$ are defined as functions of the derivatives of the hyperbolic outer product and of the derivatives of the Lorentz to Poincaré mapping. The derivatives of the hyperbolic outer product $\langle \mathbf{x}_P, \mathbf{b} \rangle = \frac{1}{2} \log \left(\frac{1 - |\mathbf{x}_P|^2}{|\mathbf{x}_P - \mathbf{b}|^2} \right)$ are given as,

$$\frac{\partial}{\partial \mathbf{x}_P} \langle \mathbf{x}_P, \mathbf{b} \rangle = -\frac{1}{2} \left(\frac{2\mathbf{x}_P}{1 - |\mathbf{x}_P|^2} + \frac{2(\mathbf{x}_P - \mathbf{b})}{|\mathbf{x}_P - \mathbf{b}|^2} \right) = \frac{\mathbf{x}_P}{|\mathbf{x}_P|^2 - 1} - \frac{\mathbf{x}_P - \mathbf{b}}{|\mathbf{x}_P - \mathbf{b}|^2}, \quad (49)$$

$$\frac{\partial^2}{\partial \mathbf{x}_P^2} \langle \mathbf{x}_P, \mathbf{b} \rangle = \frac{1}{|\mathbf{x}_P|^2 - 1} \mathbf{I}_{D_x} - \frac{2\mathbf{x}_P \mathbf{x}_P^\top}{(|\mathbf{x}_P|^2 - 1)^2} - \frac{1}{|\mathbf{x}_P - \mathbf{b}|^2} \mathbf{I}_{D_x} + \frac{2(\mathbf{x}_P - \mathbf{b})(\mathbf{x}_P - \mathbf{b})^\top}{|\mathbf{x}_P - \mathbf{b}|^4}. \quad (50)$$

Finally, the derivatives of the Lorentz to Poincaré mapping $\mathbf{x}_P = \frac{1}{1+x_0} [x_1 \dots x_D]^\top \in \mathbb{H}_P^{D_x}$ are given as,

$$\left(\frac{\partial}{\partial \mathbf{x}} \mathbf{x}_P \right)_{i,j} = \begin{cases} -\frac{x_{i+1}}{(1+x_0)^2} & j = 0 \\ \frac{1}{1+x_0} & j = i + 1 \\ 0 & \text{otherwise} \end{cases}, \quad \left(\frac{\partial^2}{\partial \mathbf{x}^2} \mathbf{x}_P \right)_{i,j,k} = \begin{cases} \frac{2x_{i+1}}{(1+x_0)^3} & j = k = 0 \\ -\frac{1}{(1+x_0)^2} & j = 0 \text{ and } k = i + 1 \\ -\frac{1}{(1+x_0)^2} & k = 0 \text{ and } j = i + 1 \\ 0 & \text{otherwise} \end{cases}, \quad (51)$$

with $i \in \{0, \dots, D_x - 1\}$, $j, k \in \{0, \dots, D_x\}$, and $D_x = 2$.

B.2. 3D Hyperbolic SE Kernel Derivatives

This section provides the derivations of the 3D hyperbolic SE kernel derivatives. Sec. 4.2 introduced the helper variables $u = \langle \mathbf{x}, \mathbf{z} \rangle_{\mathcal{L}}$ and $s = \sqrt{u^2 - 1}$ with derivatives $\frac{\partial u}{\partial \mathbf{x}} = \mathbf{G}^{\mathcal{L}} \mathbf{z}$, $\frac{du}{ds} = \frac{-1}{s}$, and $\frac{ds}{du} = \frac{u}{s}$. Using these expressions, the first and

second derivatives of the 3D hyperbolic SE kernel $k(\mathbf{x}, \mathbf{y}) = \frac{\rho}{s} e^{-\frac{\rho^2}{\nu}}$ are given as,

$$\frac{\partial}{\partial \mathbf{x}} k(\mathbf{x}, \mathbf{z}) = \left[\frac{\partial u}{\partial \mathbf{x}} \frac{d}{du} \rho \right] \frac{1}{s} e^{-\frac{\rho^2}{\nu}} + \rho \left[\frac{\partial u}{\partial \mathbf{x}} \frac{d}{du} s^{-1} \right] e^{-\frac{\rho^2}{\nu}} + \frac{\rho}{s} \left[\frac{\partial u}{\partial \mathbf{x}} \frac{d\rho}{du} \frac{d}{d\rho} e^{-\frac{\rho^2}{\nu}} \right], \quad (52)$$

$$= -\frac{1}{s^2} \mathbf{G}^{\mathcal{L}} \mathbf{z} e^{-\frac{\rho^2}{\nu}} - \frac{\rho u}{s^3} \mathbf{G}^{\mathcal{L}} \mathbf{z} e^{-\frac{\rho^2}{\nu}} + \frac{\rho}{s^2} \mathbf{G}^{\mathcal{L}} \mathbf{z} \frac{2\rho}{\nu} e^{-\frac{\rho^2}{\nu}}, \quad (53)$$

$$= g(u) e^{-\frac{\rho^2}{\nu}} \mathbf{G}^{\mathcal{L}} \mathbf{z}, \quad (54)$$

$$\frac{\partial^2}{\partial \mathbf{z} \partial \mathbf{x}} k(\mathbf{x}, \mathbf{z}) = \mathbf{G} \mathbf{z} \left[\frac{\partial u}{\partial \mathbf{z}} \frac{d}{du} g(u) \right] e^{-\frac{\rho^2}{\nu}} + \mathbf{G} \mathbf{z} g(u) \left[\frac{\partial u}{\partial \mathbf{z}} \frac{d\rho}{du} \frac{d}{d\rho} e^{-\frac{\rho^2}{\nu}} \right] + g(u) e^{-\frac{\rho^2}{\nu}} \left[\frac{\partial}{\partial \mathbf{z}} \mathbf{G} \mathbf{z} \right], \quad (55)$$

$$= \left[\frac{d}{du} g(u) \right] e^{-\frac{\rho^2}{\nu}} \mathbf{G} \mathbf{z} \mathbf{x}^{\top} \mathbf{G}^{\mathcal{L}} + g(u) \frac{-1}{s} \frac{-2\rho}{\nu} e^{-\frac{\rho^2}{\nu}} \mathbf{G} \mathbf{z} \mathbf{x}^{\top} \mathbf{G}^{\mathcal{L}} + g(u) e^{-\frac{\rho^2}{\nu}} \mathbf{G}^{\mathcal{L}}, \quad (56)$$

$$= (h(u) \mathbf{G}^{\mathcal{L}} \mathbf{z} \mathbf{x}^{\top} \mathbf{G}^{\mathcal{L}} + g(u) \mathbf{G}^{\mathcal{L}}) e^{-\frac{\rho^2}{\nu}}, \quad (57)$$

$$\frac{\partial^2}{\partial \mathbf{x} \partial \mathbf{x}} k(\mathbf{x}, \mathbf{z}) = h(u) \mathbf{G}^{\mathcal{L}} \mathbf{z} \mathbf{z}^{\top} \mathbf{G}^{\mathcal{L}} e^{-\frac{\rho^2}{\nu}}. \quad (58)$$

For the third-order derivatives, we consider each column $\mathbf{K}_j \in \mathbb{R}^{4 \times 1}$ and row $\mathbf{K}_i \in \mathbb{R}^{1 \times 4}$ of $\mathbf{K} = \frac{\partial^2}{\partial \mathbf{z} \partial \mathbf{x}} k(\mathbf{x}, \mathbf{z})$ individually, and we proceed as follows,

$$\frac{\partial}{\partial \mathbf{z}} \mathbf{K}_j = \frac{\partial}{\partial \mathbf{z}} (h(u) \mathbf{G}^{\mathcal{L}} \mathbf{z} x_j + g(u) e_j) \Delta_{1j} e^{-\frac{\rho^2}{\nu}}, \quad (59)$$

$$= \left(\left[\frac{d}{du} h(u) \right] \mathbf{G}^{\mathcal{L}} \mathbf{z} \mathbf{x}^{\top} \mathbf{G}^{\mathcal{L}} x_j + h(u) \mathbf{G}^{\mathcal{L}} x_j + \left[\frac{d}{du} g(u) \right] e_j \mathbf{x}^{\top} \mathbf{G}^{\mathcal{L}} \right) \Delta_{1j} e^{-\frac{\rho^2}{\nu}} \quad (60)$$

$$+ (h(u) \mathbf{G}^{\mathcal{L}} \mathbf{z} x_j + g(u) e_j) \Delta_{1j} \frac{2\rho}{\nu s} e^{-\frac{\rho^2}{\nu}} \mathbf{x}^{\top} \mathbf{G}^{\mathcal{L}}, \quad (61)$$

$$= (q(u) \mathbf{G}^{\mathcal{L}} \mathbf{z} \mathbf{x}^{\top} \mathbf{G}^{\mathcal{L}} x_j + h(u) \mathbf{G}^{\mathcal{L}} x_j + h(u) e_j \mathbf{x}^{\top} \mathbf{G}^{\mathcal{L}}) \Delta_{1j} e^{-\frac{\rho^2}{\nu}}, \quad (62)$$

$$\frac{\partial}{\partial \mathbf{x}} \mathbf{K}_i = (q(u) \mathbf{G}^{\mathcal{L}} \mathbf{z} \mathbf{x}^{\top} \mathbf{G}^{\mathcal{L}} z_i + h(u) \mathbf{G}^{\mathcal{L}} z_i + h(u) \mathbf{G} \mathbf{z} e_i^{\top}) \Delta_{1i} e^{-\frac{\rho^2}{\nu}}. \quad (63)$$

By stacking the row derivatives $\frac{\partial}{\partial \mathbf{x}} \mathbf{K}_i \in \mathbb{R}^{1 \times 4 \times 4}$ along the first dimension and the column derivatives $\frac{\partial}{\partial \mathbf{z}} \mathbf{K}_j \in \mathbb{R}^{4 \times 1 \times 4}$ along the second, we get the full third-order kernel derivatives $\frac{\partial}{\partial \mathbf{x}} \mathbf{K}, \frac{\partial}{\partial \mathbf{z}} \mathbf{K} \in \mathbb{R}^{4 \times 4 \times 4}$. As discussed in Sec. 4.2, automatic differentiation tools such as PyTorch cannot evaluate the helper functions $g(u)$, $h(u)$, and $q(u)$ as u approaches -1 from below. To address this issue, we replace the general function definitions with their analytical limits, when u gets too close to -1 . This is equivalent to the hyperbolic distance between the two kernel inputs falling below a predefined threshold value $\rho = \operatorname{arccosh}(-u) = d_{\mathbb{H}_{\mathbb{R}^2}}(\mathbf{x}, \mathbf{z}) \leq 1e-4$. The analytical limit expressions for the helper functions are given as

$$\lim_{u \rightarrow -1^-} g(u) = \lim_{u \rightarrow -1^-} \left(\frac{2\rho^2}{\nu s^2} - \frac{1}{s^2} - \frac{u\rho}{s^3} \right) = \frac{2}{\nu} + \frac{1}{3}, \quad (64)$$

$$\lim_{u \rightarrow -1^-} h(u) = \lim_{u \rightarrow -1^-} \left(\frac{d}{du} g(u) + \frac{g(u)2\rho}{\nu s} \right) = \frac{4}{\nu^2} + \frac{6}{3\nu} + \frac{4}{15}, \quad (65)$$

$$\lim_{u \rightarrow -1^-} q(u) = \lim_{u \rightarrow -1^-} \left(\frac{d}{du} h(u) + \frac{h(u)2\rho}{\nu s} \right) = \frac{8}{\nu^3} + \frac{8}{\nu^2} + \frac{14}{5\nu} + \frac{12}{35}. \quad (66)$$

C. Hyperbolic Pullback Geodesics

In Sec. 3.3, we described the computation of geodesics according to the hyperbolic pullback metric introduced in Sec. 3.1, 3.2. Algorithm 1 summarizes the computation of a hyperbolic pullback geodesic by minimizing (24) with Riemannian optimization.

D. Experimental Details and Additional Results

Apps. D.1-D.4 provide additional details regarding the data and GPHLVM training process for each of the experiments described in Sec. 5. App D.5 provides additional insights into the hand grasps experiment of Sec. 5.4.

Algorithm 1 Computation of hyperbolic pullback geodesics

Input: Start and end points $\mathbf{x}_1, \mathbf{x}_M \in \mathbb{H}_{\mathcal{L}}^{D_x}$ of the pullback geodesic, pullback metric $\mathbf{G}^{\mathcal{P}, \mathcal{L}}$.

Output: Pullback geodesic represented as a set of points $\{\mathbf{x}_i\}_{i=1}^M$ with $\mathbf{x}_i \in \mathbb{H}_{\mathcal{L}}^{D_x}$.

Initialization:

Initialize the pullback geodesic, e.g., as the hyperbolic geodesic from \mathbf{x}_1 to \mathbf{x}_M .

Discretize the pullback geodesic with M points $\{\mathbf{x}_i\}_{i=1}^M$.

Geodesic computation:

repeat

 Compute the curve energy E (23).

 Compute the spline energy E_{spline} .

$\mathbf{x}_2, \dots, \mathbf{x}_{M-1} \leftarrow \text{RiemannianOptStep}(E + \lambda E_{\text{spline}})$.

until convergence

D.1. C-shape

The proof-of-concept experiment on the C-shape dataset was designed as a minimalist example with a simple setup. The training data consists of $N = 1000$ two-dimensional points arranged in a C shape and scaled to fit within the unit circle. In the Euclidean case, these datapoints are used as both the latent points and the observations, so that $\mathbf{X} = \mathbf{Y} \in \mathbb{R}^{1000 \times 2}$. In the hyperbolic case, the datapoints can be interpreted as elements of the Poincaré model. We represent each latent point and observation in the Lorentz model using the Poincaré to Lorentz mapping $\mathbf{x}_{\mathcal{L}} = \frac{1}{1 - \|\mathbf{x}\|^2} [1 + \|\mathbf{x}\|^2 \quad 2\mathbf{x}^T]^T \in \mathbb{H}_{\mathcal{L}}^2$. In this proof-of-concept experiment, we manually set the kernel variance, lengthscale, and noise variance of both GPLVM and GPHLVM to $(\tau, \kappa, \sigma_y^2) = (0.7, 0.15, 0.69)$. Additionally, for the GPHLVM, we used the 2D hyperbolic SE kernel with $L = 3000$ rejection samples. We used constant zero mean for both models.

The start- and end-points of the geodesics shown in Fig. 2 correspond to one of the C-shape latent points. The geodesics are represented by $M = 25$ regularly-spaced points. Geodesics on the base Euclidean manifold correspond to straight lines from \mathbf{x}_0 to \mathbf{x}_{M-1} . In the hyperbolic case, the geodesics on the base manifold are given as $\mathbf{x}_i = \text{Exp}_{\mathbf{x}_0}(t_i \text{Log}_{\mathbf{x}_0}(\mathbf{x}_{M-1}))$ with $t_i = i/(M - 1)$ and $i = \{0, \dots, M - 1\}$. The geodesics on the base manifolds were used as initialization for the pullback geodesic optimization. To compute the pullback geodesic, we applied Riemannian Adam for 200 steps with a learning rate of 0.005, optimizing the combined loss function (24) based on both curve energy and spline energy, as introduced in Sec. 3.3. In this experiment, the curve energy and spline energy were weighted equally, i.e., $\lambda = 1$ in Eq. (23).

Finally, we generated a 110×110 grid of points to visualize the volume of the pullback metric, filtering out those points lying outside the unit circle in the hyperbolic case. Then, we evaluated the pullback metric tensor at each remaining grid point. In the Euclidean case, we computed the volume at each grid point \mathbf{x}^* by evaluating the determinant of the 2×2 pullback metric tensor, $\sqrt{\det(\mathbf{G}_{\mathbf{x}^*}^{\mathcal{P}, \mathbb{R}})}$. In the hyperbolic case, the pullback metric tensor is a 3×3 matrix that lies on the 2-dimensional tangent space, leading to one of its eigenvalues being zero. To address this, we compute the volume as the product of the two nonzero eigenvalues.

D.2. MNIST Digits

We use a subset of the MNIST dataset composed of 100 datapoints for each of the classes 0, 1, 2, 3, 6, and 9. Each datapoint is represented as a 28×28 binary image. We optimize the parameters of the GPHLVM using Riemannian Adam for 500 steps, with a learning rate of 0.05. We set a Gamma prior with concentration $\alpha = 2$ and rate $\beta = 2$ on the kernel lengthscale and a Gamma prior with concentration $\alpha = 5$ and rate $\beta = 0.8$ on the kernel variance. The embeddings are initialized using PCA.

D.3. Multi-cellular Robot Design

We consider multi-cellular robots composed of a 5×5 grid of cells. Possible cell types are empty, solid, soft, a horizontal actuator or a vertical actuator. We generate a dataset of 216 multicellular robots following the hierarchical approach of Dong et al. (2024), which we explain next for completeness. The root nodes of the hierarchy are two coarse robots composed of only vertical and only horizontal actuator cells. A component is defined as a group of cells of the same type, i.e., the root robots have a single component. Children nodes of each robot are designed by dividing large components into 2 smaller

components using K-means and by assigning a different type of cell to one of these components. This process is repeated iteratively to obtain robots with up to 8 components. This results in a tree of multi-cellular robots, with coarse-grained robots close to the roots and fine-grained robots at the leaves.

To account for the hierarchical structure associated with the tree structure of the multi-cellular robots, we incorporate graph-based priors in our GPHLVM as proposed by Jaquier et al. (2024). This is achieved by leveraging the stress loss,

$$\ell_{\text{stress}}(\mathbf{X}) = \sum_{i < j} (\text{d}_{\mathbb{G}}(c_i, c_j) - \text{d}_{\mathcal{M}}(\mathbf{x}_i, \mathbf{x}_j))^2, \quad (67)$$

to match the pairwise latent distances with the tree distances, and where c_i denotes the tree node, $\text{dist}_{\mathbb{G}}$, and $\text{dist}_{\mathcal{M}}$ are the graph distance and the geodesic distance on \mathcal{M} , respectively. Therefore, training the GPHLVM is achieved by solving,

$$\underset{\mathbf{X}}{\text{argmax}} \log p(\mathbf{Y} | \mathbf{X}, \Theta) - \gamma \bar{\ell}_{\text{stress}}(\mathbf{X}), \quad (68)$$

where γ is a parameter balancing the two losses and $\bar{\ell}_{\text{stress}}(\mathbf{X})$ is the stress loss averaged over the embeddings. We set $\gamma = 6000$. Moreover, we use a Gamma prior with concentration $\alpha = 2$ and rate $\beta = 2$ on the kernel lengthscale. We optimize the parameters of the GPHLVM using Riemannian Adam for 500 steps, with a learning rate of 0.05.

D.4. Hand Grasps Generation

For the hand grasp experiment, we used data from the KIT Whole-Body Motion Database (Mandery et al., 2016). The dataset consists of 38 trajectories, with motion recordings from two human subjects (IDs 2122 and 2123). Each subject performed 19 different grasp types¹ of the GRASP taxonomy (Feix et al., 2016). Each grasp consists of the subject grasping an object from a table, lifting it, and placing it back.

We applied several preprocessing steps to the recorded data before training the GPHLVM model: (1) We applied a low-pass filter to remove high-frequency noise; (2) We trimmed the start and end of each trajectory to focus solely on the motion from the initial resting pose to the point where the grasp was completed. Since detecting the exact point of grasp completion is non-trivial, we cut off the trajectories at the moment when the grasped object was first moved by the subject; (3) We subsample the trajectories; and (4) We centered the data to allow for the use of a zero mean function in the GPHLVM model. After preprocessing, each trajectory is composed of 30 to 40 data points. Stacking all trajectories together results in a total of $N = 1321$ data points $\mathbf{Y} \in \mathbb{R}^{1321 \times 24}$.

In contrast to the previous experiments, this experiment involves trajectory data. To preserve the trajectory structure during training, we incorporated a dynamics prior $p(\mathbf{X}_{2:N} | \mathbf{X}_{1:N-1})$, similar to Wang et al. (2008), but using the wrapped Gaussian distribution (38). We also used back constraints $\mathbf{X} = k(\mathbf{Y}, \mathbf{Y})\mathbf{C}$, which allow for a smooth mapping from the observation space to the latent space. The back-constraints kernel is defined as a Euclidean SE kernel with variance $\tau = 1$ and a lengthscale $\kappa = 0.4$. Moreover, each grasp type is identified with a lead node of the quantitative taxonomy of hand grasps (Stival et al., 2019). More specifically, the first point of each trajectory, which corresponds to the resting state, is assigned to the root node c_0 of the taxonomy graph, and the last point to the taxonomy node representing the corresponding grasp type. The taxonomy node c_{14} , for instance, represents the stick grasp. The number of edges between different grasp types in the taxonomy graph defines a distance function, $\text{d}_{\mathbb{G}}(c_i, c_j)$. To account for the hierarchical structure associated with the taxonomy, we additionally incorporate graph-based priors in our GPHLVM as proposed by Jaquier et al. (2024). This is achieved by leveraging the stress loss (67) to match the pairwise latent distances with the graph distances. During training, we minimize the stress loss over the first and last latent points of each trajectory along with maximizing the GPHLVM marginal likelihood by optimizing,

$$\underset{\mathbf{X}}{\text{argmax}} \log p(\mathbf{Y} | \mathbf{X}, \Theta) + 2 \frac{D_y}{D_x} \log p(\mathbf{X}_{2:N} | \mathbf{X}_{1:N-1}) - D_y \ell_{\text{stress}}(\mathbf{X}). \quad (69)$$

We performed the optimization using Riemannian Adam for 10000 steps, with a learning rate of 0.001.

As GPLVMs are generally prone to local optima during training, they benefit from a good initialization. Therefore, we initialize the first and last latent points of each trajectory to minimize the stress loss, i.e.,

$$\mathbf{X}_{\text{init}} = \min_{\mathbf{X}} \ell_{\text{stress}}(\mathbf{X}). \quad (70)$$

¹The three-finger sphere grasp of the GRASP taxonomy (Feix et al., 2016) is missing from the dataset.

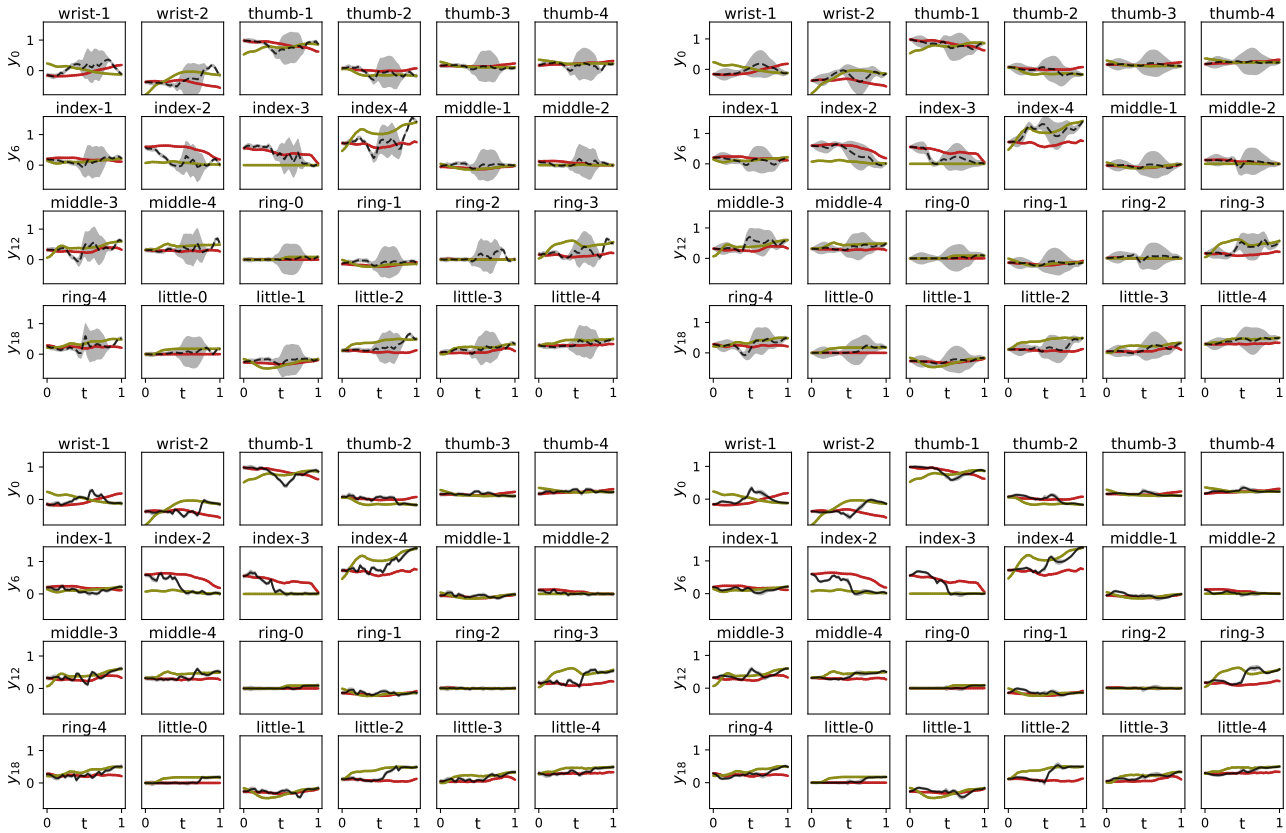


Figure 7: Time-series plots of all 24 dimensions of the joint space introduced in Fig. 5. The left and right columns show the decoded geodesics of the 2D and 3D latent spaces. The top and bottom rows show the mean of the decoded hyperbolic (- -) and pullback geodesics (—) and their uncertainty as a gray envelope. For reference, the same training trajectory to the spherical grasp (—) and reversed training trajectory from the ring grasp (—) are included.

The optimized first and last points are then connected using a hyperbolic geodesic with the same number of points as the original motion recording. To ensure distinct initialization for each subject, we added random noise to the geodesics.

For the geodesic optimization, we selected the final points of two trajectories for generating a motion from a ring grasp to a spherical grasp. We compared the hyperbolic geodesic with the pullback geodesic. Since the latent space in this experiment captures the taxonomy structure, we incorporated the expected path along the taxonomy nodes into the initialization for the pullback geodesic. Specifically, we concatenated two hyperbolic geodesics: the first connecting the spherical grasp to the origin which represents the root node of the taxonomy graph, and the second connecting the origin to the ring grasp. Starting from this initialization, we applied Riemannian Adam to optimize the geodesic over 200 steps, using a learning rate of 0.005 and a spline energy weighting of $\lambda = 100$.

D.5. Additional Hand Grasps Results

This section provides further insights into the hand grasps experiment described in Sec. 5.4. First, we present additional visualizations of the decoded geodesics. While Fig. 5 only showed 2 dimensions of the joint space, Fig. 7 depicts the decoded geodesics across all 24 dimensions, i.e., over the 24 degrees of freedom (DoF) of the hand model introduced in Mandery et al. (2016). This model counts two joints for the wrist, four joints for each finger, and two additional joints for the ring and little fingers to allow a better fist closure.

Second, we compare the GPLVM and geodesics generated in Sec. 5.4 to their counterpart Euclidean models. We train two GPLVMs augmented with a taxonomy graph prior and a dynamic prior similarly as the GPLVMs of Sec. 5.4. Fig. 8 show the resulting 2D and 3D latent spaces, alongside the Euclidean and Euclidean pullback geodesic interpolating from a ring to a spherical grasps and their corresponding decoded hand motions.

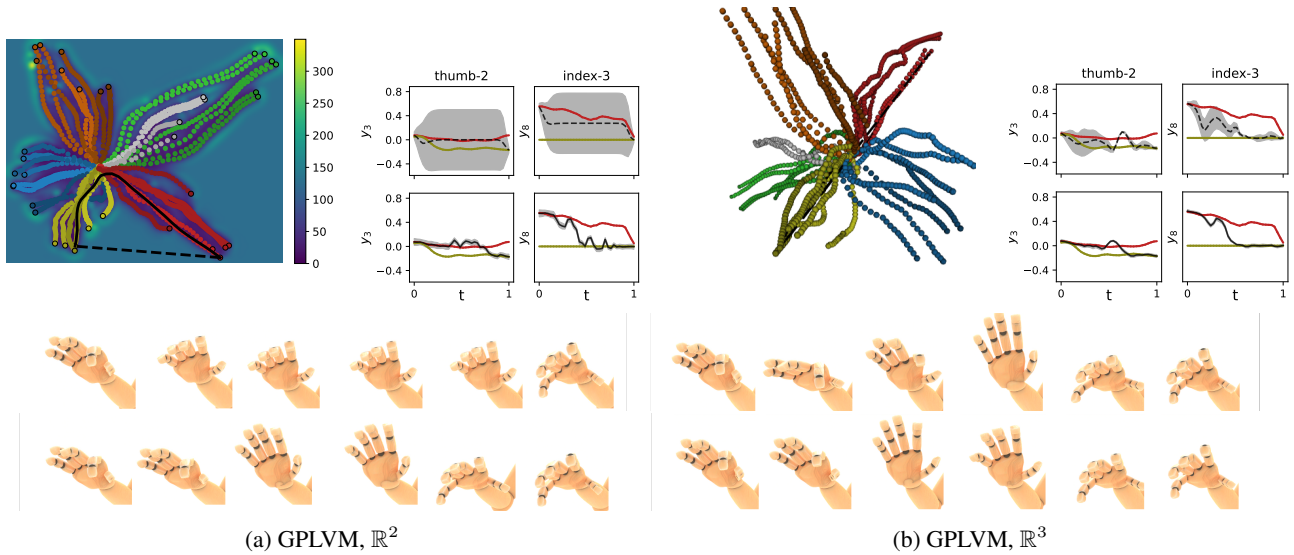


Figure 8: Hand grasps transition from a ring (\bullet) to a spherical grasp (\circ) using Euclidean ($- -$) and pullback (—) geodesics in (a) \mathbb{R}^2 and (b) \mathbb{R}^3 . *Top left*: Latent embeddings. The latent trajectory points are colored according to their corresponding grasp class. The background color in \mathbb{R}^2 represents the pullback metric volume. *Top right*: Time-series plots of 2 dimensions of the joint space. The top and bottom rows show the mean of the decoded hyperbolic ($- -$) and pullback geodesics (—) with their uncertainty as a gray envelope. A training trajectory to the spherical grasp (—) and a reversed training trajectory from the ring grasp (—) are included for reference. *Bottom*: Generated hand trajectories from the decoded hyperbolic (top) and pullback (bottom) geodesics.

Third, we discuss the influence of initialization on optimizing the pullback geodesics. As described in Sec. D.4, we initialize the pullback geodesic with two concatenated hyperbolic geodesics: One from the ring grasp to the origin and another from the origin to the spherical grasp. This initialization incorporates knowledge about the expected path in the taxonomy graph. In contrast, Fig. 9 shows the optimized pullback geodesics when the optimization is initialized solely with a hyperbolic geodesic from the ring grasp to the spherical grasp. In the two-dimensional case, we observe that the optimized pullback geodesic path differs significantly from the one shown in Fig. 5. This discrepancy is likely due to the geodesic optimization getting stuck in a local minimum, which may be a consequence of the Monte Carlo approximation of the 2D hyperbolic SE kernel. Interestingly, the three-dimensional pullback geodesic does not exhibit this issue, further supporting the hypothesis that the Monte Carlo approximation may be responsible since the 3D case does not rely on this approximation. In the 3D case, the optimized pullback geodesic follows a path very similar to the one shown in Fig. 5.

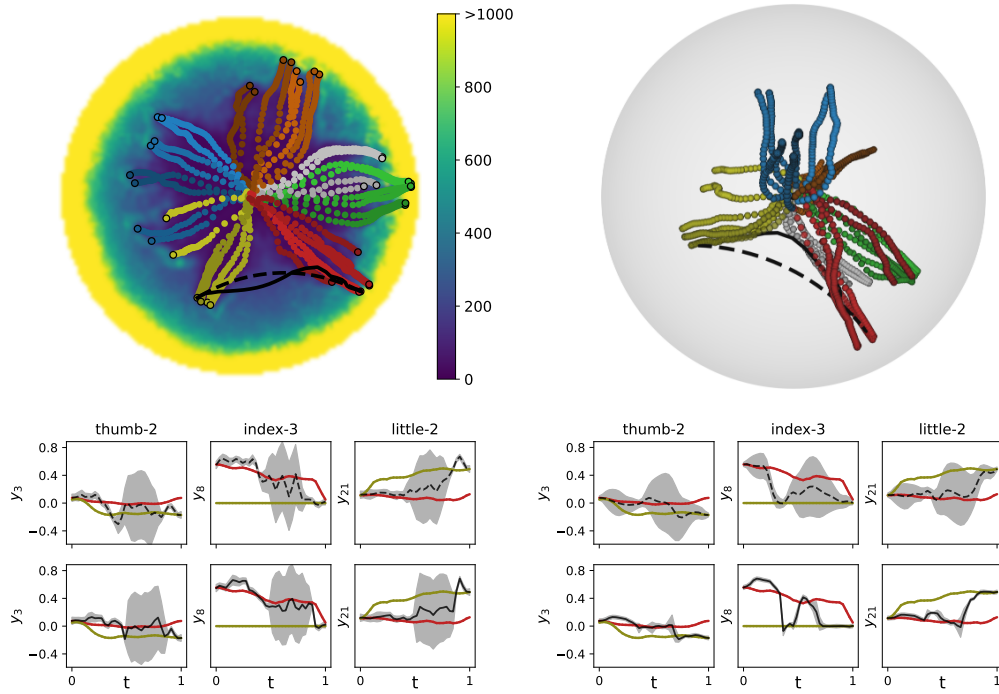


Figure 9: Hand grasps transition when initializing the geodesic optimization with the hyperbolic geodesic. As in Fig. 5, a transition from a ring (●) to a spherical grasp (●) is obtained using hyperbolic (---) and pullback (—) geodesics in $\mathbb{H}_{\mathcal{L}}^2$ (left) and $\mathbb{H}_{\mathcal{L}}^3$ (right). *Top*: 2D and 3D latent spaces of the trained models. *Bottom*: Time-series plots of 3 dimensions of the joint space for the decoded hyperbolic geodesic (---) and pullback geodesic (—).